Journal of African Earth Sciences 194 (2022) 104620

Contents lists available at ScienceDirect

Journal of African Earth Sciences

journal homepage: www.elsevier.com/locate/jafrearsci

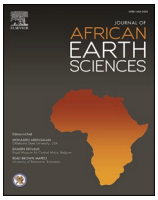

# Styles of Fe–Ti–V ore deposits in the Neoproterozoic layered mafic-ultramafic intrusions, south Eastern Desert of Egypt: Evidence for fractional crystallization of V-rich melts

Mohamed Zaki Khedr [a,*], Eiichi Takazawa [b], Shoji Arai [c], Robert J. Stern [d], Tomoaki Morishita [c], Amr El-Awady [e]

[a] Department of Geology, Faculty of Science, Kafrelsheikh University, 33516, Kafrelsheikh, Egypt
[b] Geology Department, Faculty of Science, Niigata University, Niigata, 950-2181, Japan
[c] Department of Earth Sciences, Kanazawa University, Ishikawa, 920-1192, Japan
[d] Geosciences Department, University of Texas at Dallas, Richardson, TX, 75083-0688, USA
[e] Geology Department, Faculty of Science, Zagazig University, Zagazig, 44519, Egypt

ARTICLE INFO

*Keywords:*
Fe–Ti–V oxide Deposits
Fractional crystallization
Liquid immiscibility
Ferropicritic/ferrobasaltic melts
Korab Kansi
Abu Ghalaga

ABSTRACT

The Korab Kansi and Abu Ghalaga Neoproterozoic mafic-ultramafic intrusions in the South Eastern Desert (SED) of Egypt host economic Fe–Ti–V oxide deposits, ~41 million tons for Abu Ghalaga ores. The Korab Kansi deposits are composed of titanomagnetite with subordinate ilmenite layers in dunites, gabbros and troctolites. The Abu Ghalaga ores consist of hemo-ilmenite and ilmenite with subordinate magnetite and titanomagnetite lenses in norites, gabbros and anorthosites. The difference in calculated oxygen fugacity ($f_{O2}$: ~ ΔFMQ–1.24 to −3.28 for Korab Kansi ores and +0.21 to −0.3 for Abu Ghalaga ores) during subsolidus re-equilibration is consistent with different dominant iron and titanium oxides, magnetite and hematite, respectively. Ilmenite in both deposits is enriched in Nb, Ta, Zr, Hf and V, but is poor in Cr and Ni relative to coexisting magnetite, which belongs to magmatic Fe–Ti–V deposits. The Korab Kansi and Abu Ghalaga ore deposits are rich in Ti, Fe, V, Nb, Ta and Hf with subordinate S, Cu, Ga and Zn at high $f_{O2}$. The Abu Ghalaga gabbroic intrusion crystallized from ferrobasaltic magmas of tholeiitic affinity at lower temperature (~1082 °C) and pressure (5.1 kbar) than the Korab Kansi intrusion (~1180 °C, 8.3 kbar). The Korab Kansi ore deposits mainly formed by fractional crystallization of olivine followed by in situ crystallization of Fe–Ti oxides from ferropicritic/ferrobasaltic parent melts at the floor of the magma chamber. The Abu Ghalaga ores formed as a result of more advanced fractional crystallization of ferrobasaltic parent melts. The Abu Ghalaga Fe–Ti oxides in massive ores at the base of the intrusion grew in situ, whereas most ore lenses in the middle to the top of the intrusion precipitated from immiscible oxide melts that separated from the parental magma in association with floatation of plagioclase and sulfide crystals at a late magmatic stage. Both Fe–Ti ore deposits formed from similar mantle-derived magmas but Korab Kansi ores formed as early fractionates, whereas Abu Ghalaga ores formed late. The Korab Kansi ilmenite is rich in vanadium (up to 3.8 wt% $V_2O_5$) relative to that of other magmatic deposits. Its parental melt may have formed from locally Fe–Ti–V enriched part of the Neoproterozoic mantle due to interaction with upwelling asthenosphere or a mantle plume. Controlling factors for formation of economic SED Fe–Ti–V deposits were the V-rich ferropicritic/ferrobasaltic compositions of the parental magmas, and addition of $H_2O$ to cause high magma $f_{O2}$.

## 1. Introduction

Fe–Ti–V oxide ores are orthomagmatic deposits composed mainly of ilmenite and magnetite. They are mostly hosted in layered mafic intrusions such as the Skaergaard intrusion in Greenland (Jang and Naslund, 2003), the Emeishan Large Igneous Province in SW China (Zhou et al., 2005; Liu et al., 2015), the Sept Iles layered intrusion in Canada (Namur et al., 2010, 2011, 2012), the Bushveld Complex in South Africa (Maila, 2015; Scoon et al., 2017) and Khamal gabbro-anorthosite complex (Saudi Arabia) in the Arabian Shield

* Corresponding author.
*E-mail address:* mohamed.khader1@sci.kfs.edu.eg (M.Z. Khedr).

https://doi.org/10.1016/j.jafrearsci.2022.104620
Received 14 January 2022; Received in revised form 19 May 2022; Accepted 9 June 2022
Available online 11 June 2022

(Eldougdoug et al., 2020). Fe–Ti oxide ores and associated silicate layers are generated by several magmatic processes, including segregation of immiscible Fe–Ti±P±V-rich magma, fractional crystallization by in situ crystallization and/or crystal settling of oxides, magma mixing, polybaric crystallization and solid-state remobilization (Campbell, 1978; McBirney and Noyes, 1979; Martin, 1990; Morisset et al., 2010; Charlier et al., 2015; Kruger and Latypov, 2020; Latypov et al., 2020).

Ferrian ilmenite or hemo-ilmenite (70% $FeTiO_3$– 30% $Fe_2O_3$; Bergeron, 1980) is ilmenite with exsolution lamellae of hematite (Basley and Buddington, 1958) and is the principal Ti ore in the largest deposits such as Lac Tio (or Allard Lake) in Quebec, Tellnes in SW Norway (Bergeron, 1980; Morisset et al., 2010; Charlier et al., 2006, 2007, 2010, 2015) and Abu Ghalaga ilmenite (this study) in the South Eastern Desert (SED) of Egypt. On the other hand, magmatic magnetite is the main source of vanadium (about 85% of the $V_2O_5$ global production) in Fe–Ti oxide deposits hosted in large layered mafic intrusions (Liu et al., 2015). Vanadium content is higher in Korab Kansi ilmenite ($V_2O_5$, up to 3.8 wt %) and magnetite ($V_2O_5$, up to 2.0 wt%) than in other global intrusions, but similar to that (2.0–2.5 wt% $V_2O_5$) in the Bushveld magnetite hosted in Fe-rich gabbros (Scoon et al., 2017), and the V-bearing (1.93–2.68 wt % $V_2O_5$) magnetite and ilmenite mineralization from the Sinarsuk, West Greenland (Grammatikopoulos et al., 2002). Consequently, the Korab Kansi layered intrusion with high vanadium is worth studying for understanding formation conditions of high-vanadium Fe–Ti oxide deposits.

Fe–Ti oxide deposits are hosted in few layered mafic-ultramafic intrusions in the SED of Egypt, especially the Abu Ghalaga and Korab Kansi intrusions (Fig. 1a). They are composed mainly of hemo-ilmenite, titanomagnetite, ilmenite and magnetite, similar to worldwide Fe–Ti–V oxide ores in layered mafic-ultramafic intrusions, including Sinarsuk in W.Greenland (Grammatikopoulos et al., 2002), Panzhihua in China (Zhou et al., 2005), Allard Lake in Canada (Morisset et al., 2010; Charlier et al., 2010), Mustavaara in Finland (Karinen et al., 2015) and the Khamal complex in the Arabian Shield (Eldougdoug et al., 2020). Wadi Abu Ghalaga and Gabal Korab Kansi provide the most promising of SED deposits, while Gabal Akab El Negum, Wadi Abu Fas, Gabal Kolminab, Um Effein, Wadi Rahaba, Um Ginud and Gabal El Rokham are minor occurrences (Basta and Girgis, 1968, 1969; Girgis, 1977; Sabet and Khalaf, 1989; Nasr et al., 2000). The Abu Ghalaga mine has the largest Fe–Ti ore reserves not only in Egypt but also in the Arabian-Nubian Shield, estimated to be about 41 million tons of hemo-ilmenite deposits averaging 35% $TiO_2$ (Basta and Takla, 1968).

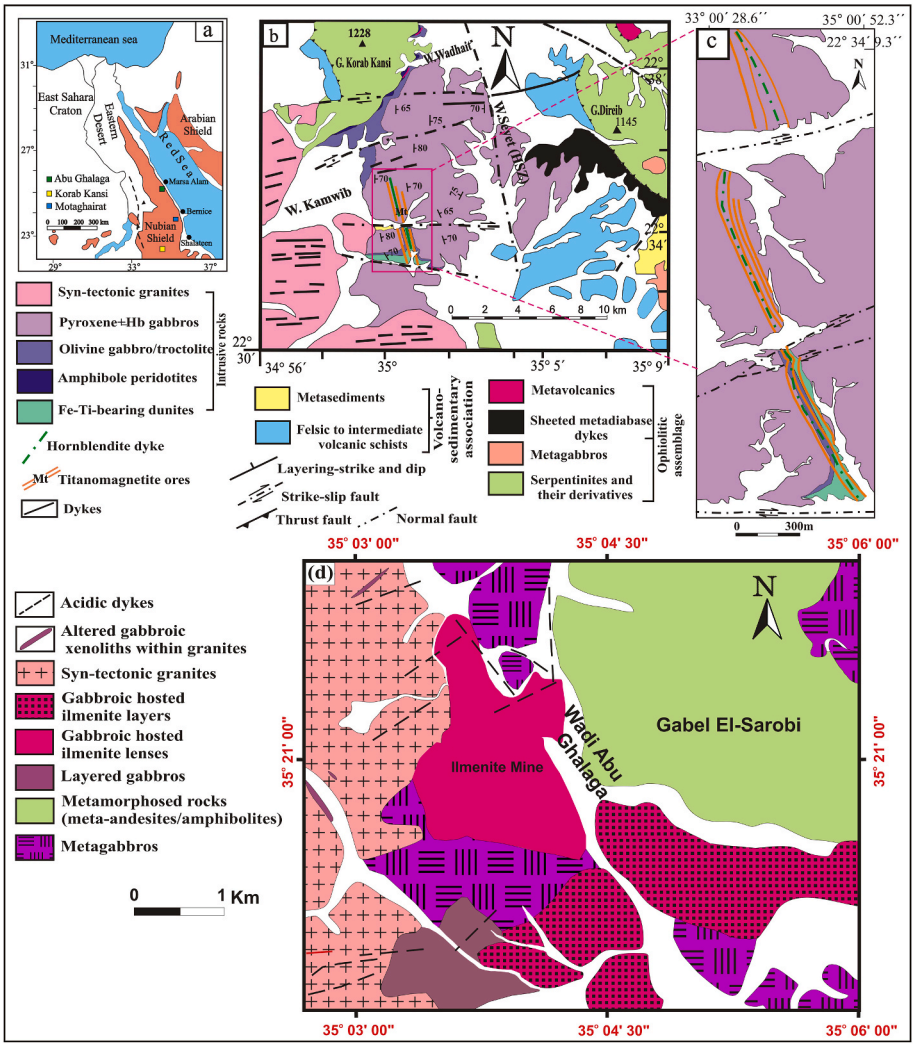


**Fig. 1.** Geological maps of Fe–Ti–V ore deposits in the South Eastern Desert of Egypt. **a**) Location of Gabal Korab Kansi and Abu Ghalaga. **b**) Korab Kansi geological map showing the distibution of different rock units (Abdel-Gawad, 2002; Khedr et al., 2020). **c**) Distribution of Fe–Ti–V oxide ore layers at south Korab Kansi (Makhlouf et al., 2008). **d**) Geological map of Abu Ghalaga area based on integration of Landsat 8 OLI (7,5 and 3 bands as RGB), MNF (4, 2 and 1 bands as RGB) and PCA (1, 2 and 3 bands as RGB) and Abu Ghalaga geological map (Amin, 1954).

These hemo-ilmenite deposits are estimated to contain 14.3 million tons of $TiO_2$, 21.3 million tons of $Fe_2O_3$ and 0.14 million tons of $V_2O_5$ (Amin, 1954; Basta and Takla, 1968; EMRA, 2014). The Korab Kansi ranks second in ore reserves with 1.8 million tons of semi-massive ore and 2.5 million tons of disseminated one (Shaaban et al., 2003). Comparison of Korab Kansi and Abu Ghalaga Fe–Ti ore deposits can provide insights on fractionation of Fe–Ti–V rich melts, magmatic differentiation processes and mechanisms of Fe–Ti–V oxide accumulation in magma chambers.

Fe–Ti–P mineralization in the Arabian-Nubian Shield (ANS) have long been noted (e.g., Amin, 1954; Basta and Takla, 1968; Basta, 1977; Eldougdoug et al., 2020), but without geochemical studies. This is the first detailed geochemical study of Neoproterozoic Fe–Ti–V oxide ores in the Nubian Shield. It deals with the field occurrence, microtextures, mineralogy and chemistry (major, trace and REE) of economic Fe–Ti–V oxide deposits in two layered mafic-ultramafic intrusions in the SED of Egypt, the Abu Ghalaga and Korab Kansi (Fig. 1, Supplementary 1). The main goal of this study is to understand the genesis of Neoproterozoic Fe–Ti–V ore deposits and to determine mechanisms of their formation. This study also aims to understand factors controlling economic Fe–Ti–V ore deposits in the SED of Egypt and to explain the enrichment of vanadium the Korab Kansi Fe–Ti oxide deposits relative to other Fe–Ti deposits.

## 2. Geological setting

The Korab Kansi layered mafic-ultramafic intrusion is located, ~350 km south of the Abu Ghalaga (Fig. 1a) in the SED of Egypt. The intrusion consists of dunite layers, amphibole peridotites, thin pyroxenites and hornblendites, troctolites, olivine gabbros, gabbronorites, pyroxene gabbros and pyroxene-hornblende gabbros. Hornblendites occur as several centimetre thick bands at the contact between Fe–Ti–V layers and gabbros (Fig. 2e). These hornblendite bands generally strike NNW-SSE, and dip steeply (70°-80°) to the east (Fig. 2 a-d; Supplementary 1a). The dunites, troctolites and olivine gabbros host economic Fe–Ti–V ore deposits in the southern part of the intrusion (Fig. 1b and c; Supplementary 1a). These ore deposits are found along the axial plane of an open fold trending 145° and gently plunging 10°–15° SE (Makhlouf et al., 2008). The Fe–Ti–V deposits display sharp contacts with host gabbros (Fig. 2a–e) and are generally concordant with the host rocks (Fig. 2c and d; Supplementary 1a), showing various thickness (1–5 m thick) in the same layer. They sometimes have green rounded patches of olivine in hand specimen (Fig. 2f) and are characterized by cumulate textures, forming Fe–Ti–V oxides-rich dunites. The Fe–Ti–V deposits are divided into three parts, separated by E-W fracture zones, and mainly show NNW-SSE and N–S trends, parallel to the Hamisana Shear Zone

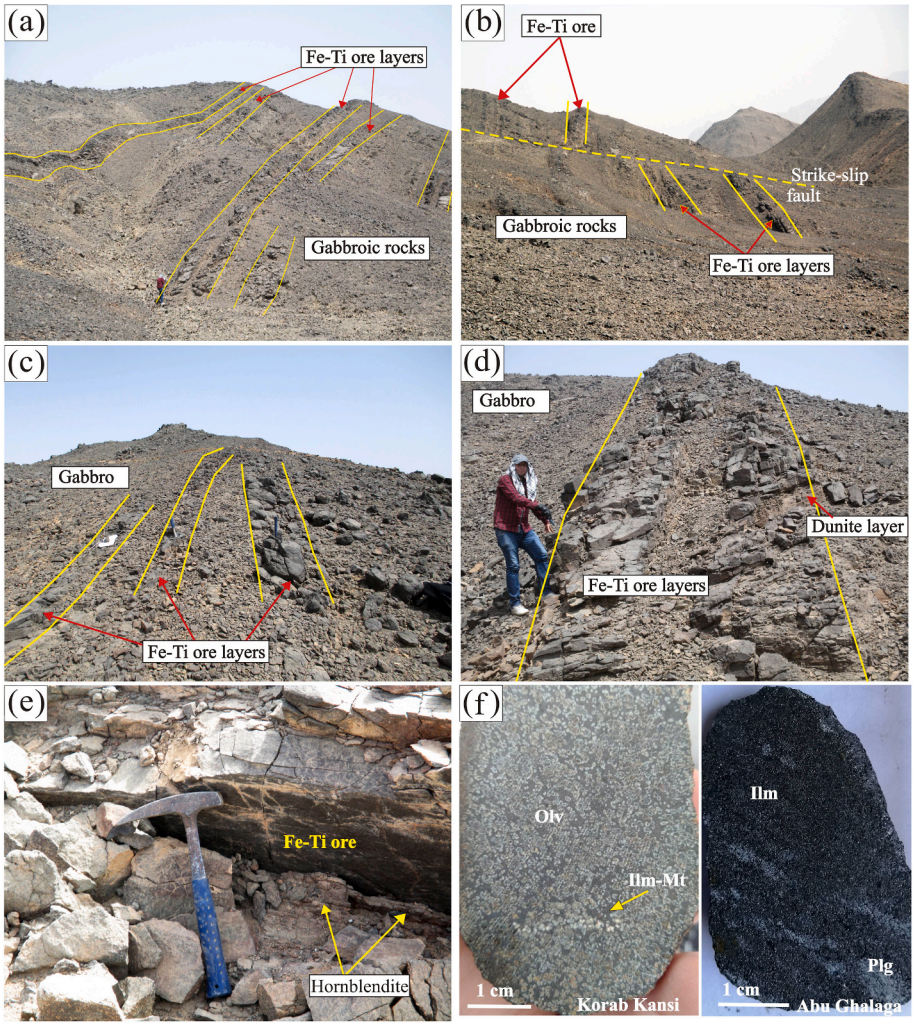


**Fig. 2.** Field photographs of Fe–Ti–V ore deposits in Korab Kansi and Abu Ghalaga layered intrusions. **a**) Parallel Fe–Ti–V oxide ore layers hosted in gabbros, with the first layer from the left showing pinch and swell structure. **b**) Multiple Fe–Ti–V oxide ore layers displaced by fault (Khedr et al., 2020) and hosted in gabbroic rocks. **c**) Partly exposed and closely spaced sill-like Fe–Ti oxide ore layers intercalated with pyroxene gabbros. **d**) Highly resistant ridge-like Fe–Ti oxide ore layer hosted in dunites with sharp or knife borders with pyroxene gabbros. **e**) Close up view of thin hornblendite layer at the contact between Fe–Ti oxide ore layers and host gabbros. **f**) Hand-sample photographs showing net-textured oxide ore with cumulus olivine in Korab Kansi semi-massive ores (left), and plagioclase aggregates in Abu Ghalaga ilmenite-rich norites (right).

**Table 1**
Representative microprobe analyses of silicates and Al-spinel in Korab Kansi and Abu Ghalaga ore layers.

| Area | Korab Kansi (Kn) | | | | Abu Ghalaga (Ghl) | | | | Kn | | Abu Ghalaga | |
|---|---|---|---|---|---|---|---|---|---|---|---|---|
| Rock Name | Fe–Ti–V oxide-rich Troctolite | Fe–Ti–V oxide-rich Dunite | | | Ilmenitite | Ilmenite-rich melanorite | Ilmenitite | Ilmenite-rich melanorite | Fe–Ti–V oxide-rich Troctolite | Fe–Ti–V oxide-rich Dunite | Ilmenitite | Ilmenite-rich melanorite |
| Sample | Kn28 | Kn25 | Kn10 | Kn25 | Ghl35 | Ghl23 | Ghl42 | Ghl23 | kn28 | Kn23 | Ghl18 | Ghl23 |
| Mineral | Olivine | | Iddingsite | | Opx | | Cpx | | Prg | Prg | Prg | Ed |
| SiO2 | 37.7 | 37.6 | 25.4 | 30.5 | 53.3 | 51.9 | 52.6 | 52.6 | 41.9 | 41.1 | 42.5 | 46.6 |
| TiO2 | 0.00 | 0.06 | 0.05 | 0.06 | 0.32 | 0.10 | 0.44 | 0.24 | 3.77 | 3.91 | 0.88 | 1.92 |
| Al2O3 | 0.00 | 0.00 | 0.02 | 0.05 | 1.6 | 1.9 | 2.3 | 1.7 | 13.3 | 13.7 | 15.5 | 8.9 |
| Cr2O3 | 0.00 | 0.00 | 0.00 | 0.00 | 0.04 | 0.00 | 0.00 | 0.05 | 0.00 | 0.00 | 0.00 | 0.00 |
| FeO | 26.9 | 24.3 | 50.7 | 39.8 | 15.3 | 21.8 | 5.5 | 7.9 | 10.5 | 8.8 | 8.5 | 10.5 |
| MnO | 0.32 | 0.36 | 0.15 | 0.36 | 0.27 | 0.38 | 0.07 | 0.21 | 0.11 | 0.02 | 0.12 | 0.11 |
| MgO | 35.3 | 38.3 | 11.1 | 9.4 | 26.6 | 22.9 | 15.8 | 14.4 | 13.2 | 13.8 | 14.9 | 15.6 |
| NiO | 0.02 | 0.03 | 0.81 | 0.84 | 0.00 | 0.00 | 0.00 | 0.00 | 0.00 | 0.00 | 0.04 | 0.00 |
| CaO | 0.00 | 0.06 | 0.09 | 0.26 | 2.3 | 0.8 | 22.7 | 22.3 | 11.1 | 11.8 | 11.2 | 11.6 |
| Na2O | 0.00 | 0.00 | 0.00 | 0.34 | 0.05 | 0.02 | 0.42 | 0.37 | 3.03 | 3.15 | 2.34 | 1.30 |
| K2O | 0.00 | 0.00 | 0.12 | 0.05 | 0.00 | 0.00 | 0.00 | 0.00 | 0.67 | 0.61 | 0.11 | 0.48 |
| BaO | 0.00 | 0.00 | 0.00 | 0.00 | 0.04 | 0.00 | 0.03 | 0.00 | 0.00 | 0.00 | 0.03 | 0.08 |
| Total | 100.2 | 100.8 | 88.4 | 81.7 | 99.8 | 99.8 | 99.8 | 99.8 | 97.7 | 97.0 | 96.2 | 97.1 |
| Fo | 69.84 | 73.43 | – | – | 75.66 | 65.23 | 83.65 | 76.51 | – | – | – | – |
| An | – | – | – | – | – | – | – | – | – | – | – | – |
| Mg# | – | – | – | – | – | – | – | – | 0.72 | 0.74 | 75.74 | 72.53 |

Olv: olivine, Opx: orthopyroxene, Cpx: clinopyroxene, Prg: pargasite, Ed: edenite, Anth: anthophyllite, Act: actinolite, Prh: prehnite, Al-spinel: aluminium spinel. Chl: chlorite; Apt: apatite.

along Wadi Seyet (Fig. 1b and c; Supplementary 1a).

The Korab Kansi Fe–Ti–V deposits mainly occur as resistant ridge-like bodies with a few ore horizons occurring as discordant dyke-like bodies because they are disrupted or tilted by faults and folds (Fig. 2b). They are semi-massive ores with subordinate massive to disseminated types. The Korab Kansi disseminated Fe–Ti–V ores in host troctolites are found in the north, whereas semi-massive ores hosted in dunites (Fig. 2d) are found in the south. Thin bands of disseminated ores are observed along the upper parts of the massive ore body. The thickness and mode of occurrence of ore deposits vary along strike due to NW-SE compression, which caused pinch and swell structure of ore layers (Fig. 2a) (Makhlouf et al., 2008). The Fe–Ti–V deposits range from <1 to 5 m thick (Fig. 2), and are exposed for less than 2.5 km (600 m on average) along strike (Makhlouf et al., 2008), taking the form of magmatic layers (Supplementary 1a). In some locations, ore layers <1m thick are spaced less than 1 m apart (Fig. 2c).

The Abu Ghalaga Fe–Ti ores are hosted by titaniferous gabbroic rocks (Fig. 1d; Supplementary 1b) that are elongated NNE, forming the layered mafic intrusion. These titaniferous gabbroic rocks, which are mainly gabbros, gabbronorites, norites and anorthosites, are surrounded by Abu Ghalaga syn-tectonic granites and metagabbros in the west and Gebel El-Sarobi amphibolites and meta-andesites in the east (Basta and Takla, 1968) (Fig. 1d; Supplementary 1b). The Abu Ghalaga gabbroic rocks have a gradational contact with syn-tectonic granites to the west, which contain small bodies of altered gabbroic xenoliths especially in the NW part of the mapped area (Fig. 1d; Supplementary 1b). The syn-tectonic granites sometimes intrude into the gabbroic rocks, and granite porphyry dykes with E-W strike traverse ilmenite deposits and their host gabbros (Fig. 1d).

The Abu Ghalaga layered gabbroic rocks host abundant Fe–Ti ore deposits, which commonly occur as lenses, layers and veins (Fig. 1d; Supplementary 1b). A few ilmenite pods also occur as enclaves in gabbroic rocks near contacts with granites (Supplementary 1b). The Fe–Ti ore deposits are generally concordant with layered gabbros and mainly strike NW-SE and dip NE. Layering is also observed in the main ore body, where thin gabbro layers are intercalated with thicker ore bands (Supplementary 1b). Some Fe–Ti ore deposits form an inclined sheet-like feature on the top of the gabbroic mass (Amin, 1954), and display sharp contacts with host norites and anorthosites. Anorthosites contain disseminated Fe–Ti ores, mainly ilmenite with minor magnetite (Basta and Takla, 1968). Few discordant ore bodies occur as lenses or vertical dykes (50–100 cm across) crosscutting layers of norites and anorthosites that are enveloped by gabbros.

The Abu Ghalaga massive and disseminated Fe–Ti ore layers can be subdivided (Basta and Takla, 1968) into: 1) ilmenite-rich melanorites in the lower part of the intrusion (at great depth in drill holes), 2) ilmenite layers with intercalated gabbros in the middle section of the intrusion, and 3) ilmenite ore layers below and within anorthosites at the top of the intrusion. The Abu Ghalaga ores have various dimensions with a maximum exposed length of about 300 m and a thickness of more than 105 m for the main ilmenite lens. Some massive ilmenite layers are several meters long and range from less than 1 m to more than 20 m thick, whereas small ilmenite lenses (less than 20 m long) are also observed in medium-grained metagabbros to the west and northeast of the main ilmenite body (Amin, 1954; Basta and Takla, 1968; EMRA, 2014) (Fig. 1d; Supplementary 1b). On the surface of gabbroic intrusions, the main ilmenite ore lenses are capped by strongly weathered zones less than 50 cm thick. Ilmenite ores in these lenses are mainly massive (Fig. 2f), showing submetallic luster. A few ilmenite ore layers include fragments (autoliths) of norites and anorthositic gabbros (few centimetres to few meters) with sharp contacts (Basta and Takla, 1968).

## 3. Analytical methods

We collected 73 and 42 samples from Korab Kansi and Abu Ghalaga mafic-ultramafic intrusions, respectively. All samples were prepared as polished thin sections for petrography and mineral chemistry. Major-element compositions of silicate minerals (e.g. olivine, pyroxene,

| Abu Ghalaga | | Korab | Abu Ghalaga | | Kn | | Ghl | Korab Kansi | | Ghl |
|---|---|---|---|---|---|---|---|---|---|---|
| Ilmenitite | Ilmenite-rich norite | Fe–Ti–V oxide-rich Dunite | Altered Ilmenitite | | Fe–Ti–V oxide-rich Troctolite | Fe–Ti–V oxide-rich Dunite | Ilmenite-rich norite | Fe–Ti–V oxide-rich Dunite | | Ilmenite-rich norite |
| Ghl18 | Ghl24 | Kn5 | Ghl10 | | Kn28 | Kn23 | Ghl38 | Kn23 | Kn10 | Ghl24 |
| Anth | Act | Chl | Serp | Talc | Plagioclase | | | Prh | Al-Spl | Apt |
| 53.4 | 54.3 | 26.9 | 46.8 | 61.6 | 53.7 | 53.6 | 51.9 | 40.8 | 0.4 | bdl |
| 0.22 | 0.29 | 0.16 | 0.10 | 0.13 | bdl | 0.06 | 0.07 | 0.09 | 0.00 | 0.03 |
| 4.4 | 3.1 | 20.1 | 4.9 | 1.3 | 28.9 | 29.3 | 29.9 | 29.5 | 62.6 | 0.0 |
| 0.04 | 0.00 | 21.15 | 0.00 | 0.00 | 0.00 | 0.00 | 0.00 | 0.00 | 0.56 | 0.00 |
| 12.4 | 7.1 | 0.0 | 5.0 | 3.8 | 0.2 | 0.0 | 0.2 | 1.7 | 22.0 | 0.1 |
| 0.24 | 0.09 | 18.05 | 0.00 | 0.02 | 0.00 | 0.00 | 0.00 | 0.65 | 0.14 | 0.01 |
| 24.5 | 20.0 | 0.0 | 27.6 | 28.0 | 0.0 | 0.0 | 0.0 | 0.0 | 14.1 | 0.0 |
| 0.02 | 0.00 | 0.00 | 0.14 | 0.02 | 0.00 | 0.00 | 0.00 | 0.00 | 0.07 | 0.00 |
| 0.5 | 11.3 | 0.0 | 0.0 | 0.3 | 11.8 | 11.4 | 11.1 | 24.0 | 0.0 | 55.4 |
| 0.55 | 0.31 | 0.18 | 0.12 | 0.00 | 4.99 | 5.03 | 5.33 | 0.02 | 0.02 | 0.02 |
| 0.00 | 0.00 | 0.07 | 0.00 | 0.00 | 0.03 | 0.03 | 0.02 | 0.00 | 0.00 | 0.00 |
| 0.00 | 0.01 | 0.00 | 0.00 | 0.04 | 0.00 | 0.00 | 0.00 | 0.00 | 0.00 | 0.01 |
| 96.2 | 96.4 | 86.7 | 84.6 | 95.2 | 99.6 | 99.5 | 98.6 | 96.9 | 100.0 | 55.6 |
| – | – | – | – | | – | – | – | – | – | – |
| – | – | – | – | | 56.55 | 55.45 | 53.43 | – | – | – |
| 77.94 | 83.37 | – | 0.91 | 0.93 | – | – | – | – | – | – |

amphiboles, plagioclase, prehnite, chlorite, serpentine, talc and iddingsite), oxides (e.g. ilmenite, titanomagnetite, magnetite, titanohematite and Al-rich spinel) and sulfides (Tables 1 and 2; Supplementarys 2–4) in Korab Kansi Fe–Ti-rich rocks were determined using a JEOL wavelength dispersive electron probe X-ray micro-analyzer (EPMA: JXA 8800R) at Kanazawa University, Japan. Analysis conditions were 20 kV for accelerating voltage, 20 nA for the beam current and 3-μm beam diameter. The values of Si, Cr, Fe, Ca, (K, Ti), Al, Mn, Na, Ni and Mg were determined and calibrated on the standards: quartz, eskolaite, fayalite, wollastonite, $KTiPO_5$, corundum, manganosite, jadite, nickel oxide and periclase, respectively. The detection limits (ppm) calculated by the microprobe soft-ware are Si (123), Cr (320), Fe (195), Ca (115), K (98), Ti (199), Al (117), Mn (198), Na (138), Ni (178) and Mg (119). Back-scattered electron (BSE) images were captured using the same conditions. Twelve samples of the Abu Ghalaga Fe–Ti oxide minerals, sulfides and coexisting gangue minerals were determined using an electron probe microanalyzer with wavelength dispersive X-ray spectrometry (JEOL JXA-8600SX) at Niigata University, Japan. Operating conditions were 15 kV accelerating voltage, 13 nA beam current, and ~1 mm beam diameter, using oxide ZAF matrix correction. Precision and accuracy of most major elements (>2.0 wt%) determined by EPMA is mainly <1%–4%, calculated based on the standards values, net intensity and background counts. Elemental distribution maps (Supplementary 6) and analyses of the Fe–Ti–V oxide minerals were carried out by Scanning Electron Microscopy (SEM)-Energy Dispersive X-Ray Spectroscopy (EDS) at Niigata University, Japan. Operating conditions were 20 kV accelerating voltage, and working distance (WD) was 10 mm.

Trace-element concentrations in olivine, iddingsite, amphiboles, plagioclase, magnetite, titanomagnetite, and ilmenite (Table 3; Supplementary 5) from Korab Kansi and Abu Ghalaga Fe–Ti-rich rocks were determined in-situ by laser ablation-inductively coupled plasma-mass spectrometry (LA-ICP-MS) using a quadrupole ICP–MS (Agilent 7500a) coupled to a 213 nm Nd:YAG laser ablation system (New Wave Research UP213) at Niigata University, Japan. Thin sections were ablated in a small cell by using the helium gas mixed with argon and nitrogen prior to entering the plasma. Analyses were performed at 4 Hz with an energy density of 10 J/cm2 per pulse and ablating 80-μm diameter spots for all minerals, except the Abu Ghalaga ilmenite with laser diameter spots of 40-μm. The total time of data acquisition for one spot is 105 s including laser ablation for 45 s and background for 40 s. Sensitivity variation during the analytical runs was corrected using five internal standards. The CaO and $SiO_2$ contents of silicates as well as $Al_2O_3$, $Fe_2O_3$ and $TiO_2$ of Fe–Ti oxides determined by electron microprobe were used as internal standards. SRM 612 and SRM 610 (Pearce et al., 1997) were used as external standards for calibrating trace element concentrations. The accuracy and data quality based on the above reference materials, assuming the composition given by Pearce et al. (1997) and multiple analysis (n = 15) of the R-185 Cpx standard, are high and acceptable. Precision or reproducibility is better than 12% for trace elements, except Zn, Rb, Cs, Ba, Ta, Pb, U and Th for which it is better than 15%.

## 4. Petrography of Fe–Ti–V oxide mineralization

The Korab Kansi Fe–Ti–V oxide ores occur as disseminated (~15–40 vol% oxides) ores in troctolites and as semi-massive (~40–70 vol%) deposits in dunites. The semi-massive ores show brownish black colors with variable amounts of olivine (Fig. 2e and f). The Fe–Ti–V oxides are found as intercumulus phases between olivine (Fig. 3a, f), iddingsite, plagioclase, serpentine and chlorite (Fig. 3a–d). Cumulus olivine (Fig. 2f) occurs as rounded equigranular crystals (up to 3 × 2.5 mm), and is mostly altered to iddingsite, serpentine and chlorite (Fig. 3a and b). Plagioclase associated with olivine occurs as cumulus crystals that are corroded by intercumulus oxide minerals (Fig. 3b and c). Plagioclase crystals are surrounded by thin reaction rims of hornblende or pargasite at the contact with Fe–Ti–V oxides (Fig. 3c). A few plagioclase crystals in the host Fe-rich gabbroic rocks show zoning and enclose chadacrysts of Fe–Ti oxides, like clinopyroxene and pargasite (Fig. 3d). The Fe–Ti–V oxides consist mainly of titanomagnetite with subrodinate ilmenite and magnetite, although minor hematite and Al-rich spinel are also observed (Fig. 3e–h). Titanomagnetite grains (0.2–2.0 mm) sometimes includes exsolved ilmenite and spinel lamellae (Fig. 3g and h) or granule (Fig. 3e). It is sometimes martitized to hematite lamellae along its octahedral cleavage planes and along its periphery (Fig. 3e, h). Large titanomagnetite grains (2.0–4.5 mm) occur between cumulus olivine

**Table 2**
Representative microprobe analyses of magnetite, titanomagnetite, titanohematite and ilmenite in Korab Kansi and Abu Ghalaga ore layers.

| Area | Korab Kansi | | | | | | | | Abu Ghalaga | | Korab Kansi | | | | Abu Ghalaga | | | | | | |
|---|---|---|---|---|---|---|---|---|---|---|---|---|---|---|---|---|---|---|---|---|---|
| Rock N. | Fe–Ti–V oxide-rich troctolite | Fe–Ti–V oxide-rich Dunite | | | | | | | Ilmenite-rich norite | Ilmenite | Fe–Ti–V oxide-rich troctolite | Fe–Ti–V oxide-rich Dunite | | | Ilmenite | | Ilmenite-rich melanorite | Ilmenite-rich norite | Ilmenite | Ilmenite-rich melanorite | Ilmenite-rich norite |
| Sample | Kn28 | Kn23 | Kn13 | Kn5 | Kn10 | Kn12 | Kn12 | Kn13 | Ghl24 | Ghl35 | Kn28 | Kn23 | Kn13 | Kn5 | Ghl18 | Ghl38 | Ghl23 | Ghl24 | Ghl18 | Ghl23 | Ghl24 |
| Mineral | Magnetite | | | | Titanomagnetite | | | | | | Ilmenite | | | | | | | | Titanohematite | | |
| SiO2 | 0.00 | 0.00 | 0.00 | 0.00 | 0.08 | 0.00 | 0.00 | 0.00 | 0.08 | 0.08 | 0.00 | 0.16 | 0.00 | 0.00 | 0.01 | 0.05 | 0.04 | 0.08 | 0.08 | 0.05 | 0.04 | 0.09 |
| TiO2 | 0.89 | 2.50 | 0.67 | 0.79 | 6.97 | 7.70 | 11.48 | 4.53 | 2.95 | 5.91 | 51.50 | 51.18 | 54.12 | 52.70 | 49.78 | 50.18 | 48.25 | 47.39 | 13.02 | 13.07 | 31.41 | 12.87 |
| Al2O3 | 1.01 | 0.62 | 0.11 | 0.29 | 2.43 | 3.22 | 2.33 | 0.16 | 0.11 | 0.16 | 0.04 | 0.02 | 0.02 | 0.03 | 0.03 | 0.02 | 0.02 | 0.00 | 0.20 | 0.06 | 0.05 | 0.08 |
| Cr2O3 | 0.53 | 0.82 | 0.63 | 1.04 | 0.62 | 0.59 | 0.64 | 0.65 | 0.20 | 0.05 | 0.00 | 0.04 | 0.00 | 0.05 | 0.00 | 0.10 | 0.09 | 0.04 | 0.33 | 0.20 | 0.17 | 0.11 |
| FeOt | 86.50 | 88.15 | 87.89 | 89.20 | 86.30 | 81.89 | 76.83 | 85.26 | 88.72 | 86.25 | 45.25 | 44.19 | 41.37 | 45.44 | 44.97 | 46.89 | 48.64 | 50.85 | 75.31 | 76.36 | 63.04 | 77.70 |
| MnO | 0.00 | 0.09 | 0.04 | 0.05 | 0.33 | 0.17 | 0.33 | 0.18 | 0.00 | 0.24 | 0.84 | 0.82 | 1.38 | 1.02 | 0.27 | 0.30 | 0.35 | 0.29 | 0.00 | 0.00 | 0.13 | 0.05 |
| MgO | 0.10 | 0.24 | 0.27 | 0.07 | 0.77 | 1.13 | 0.87 | 1.07 | 0.02 | 0.21 | 0.64 | 1.98 | 1.27 | 0.05 | 3.02 | 2.01 | 1.51 | 0.07 | 0.38 | 0.22 | 0.39 | 0.03 |
| NiO | 0.03 | 0.00 | 0.00 | 0.00 | 0.02 | 0.03 | 0.07 | 0.00 | 0.00 | 0.09 | 0.00 | 0.03 | 0.00 | 0.00 | 0.05 | 0.00 | 0.00 | 0.03 | 0.00 | 0.03 | 0.04 | 0.00 |
| BaO | 0.00 | 0.00 | 0.00 | 0.00 | 0.00 | 0.00 | 0.00 | 0.00 | 0.04 | 0.05 | 0.00 | 0.00 | 0.00 | 0.00 | 0.62 | 0.54 | 0.61 | 0.56 | 0.13 | 0.08 | 0.28 | 0.10 |
| Total | 89.1 | 92.4 | 89.6 | 91.4 | 97.5 | 94.7 | 92.5 | 91.8 | 92.1 | 93.0 | 98.27 | 98.4 | 98.2 | 99.28 | 98.7 | 100.1 | 99.5 | 99.3 | 89.4 | 90.1 | 95.5 | 91.0 |
| Fe2O3 | 63.49 | 65.00 | 65.19 | 65.67 | 63.39 | 60.21 | 56.52 | 64.38 | 65.62 | 64.10 | 1.01 | 2.6 | 0.0 | 0.00 | 6.5 | 6.2 | 9.2 | 9.5 | 67.38 | 68.09 | 35.02 | 69.29 |
| FeO | 29.37 | 29.66 | 29.23 | 30.11 | 29.25 | 27.72 | 25.97 | 27.33 | 29.67 | 28.57 | 44.34 | 41.9 | 41.5 | 46.04 | 39.1 | 41.3 | 40.4 | 42.3 | 14.68 | 15.08 | 31.52 | 15.35 |
| Xusp % | 2.75 | 7.39 | 1.80 | 2.34 | 20.21 | 23.05 | 35.08 | 12.47 | 8.79 | 17.14 | – | – | – | – | – | – | – | – | – | – | – | – |
| Xilm | – | – | – | – | – | – | – | – | – | – | 0.99 | 0.88 | 0.85 | 1.00 | 0.82 | 0.86 | 0.85 | 0.90 | – | – | – | – |
| ZnO | 0.00 | 0.00 | 0.03 | 0.17 | 0.01 | 0.00 | – | – | – | – | 0.01 | 0.02 | 0.02 | 0.08 | – | – | – | – | – | – | – | – |
| CoO | 0.10 | 0.09 | 0.11 | 0.12 | 0.09 | 0.11 | – | – | – | – | 0.05 | 0.04 | 0.08 | 0.06 | – | – | – | – | – | – | – | – |
| V2O5 | 2.01 | 1.40 | 1.21 | 1.50 | 1.83 | 1.90 | – | – | – | – | 3.10 | 3.68 | 3.62 | 3.48 | – | – | – | – | – | – | – | – |

grains, forming net-textured ores (Fig. 3f) Titanomagnetite shows different textural relations with associated ilmenite such as: 1) composite grains (Figs. 3h), 2) sandwich lamellae intergrowth (Fig. 3e, h), and 3) exsolution trellis texture due to intergrowth of ilmenite lamellae with the host titanomagnetite (Fig. 3g). Sulfides are rare, and appear as fine-grained pyrrhotite and pyrite along titanomagnetite boundaries.

The Abu Ghalaga massive (>70 vol% oxides) and semi-massive ore (~40–70 vol% Fe–Ti oxides) usually contain whitish grey spots of plagioclase (Fig. 2f). They are enriched in plagioclase (15–50 vol%) and sulfides (up to 5 vol%) contents relative to Korab Kansi ores. Gangue minerals are mainly plagioclase, amphibole and orthopyroxene (Opx) with minor amounts of clinopyroxene (Cpx) and apatite (Fig. 4a–d). Their alteration products are tremolite, actinolite, anthophyllite, antigorite and talc (Fig. 4a–d). Boundaries between massive Fe–Ti oxides and anorthosites in thin section are sharp (Fig. 4a). The Abu Ghalaga ore samples can be classified into ilmenitites (>80% Fe–Ti oxides + ~15% plagioclase and Opx), ilmenite-rich anorthosites (~50–70% Fe–Ti oxides + ~30–50% plagioclase; Fig. 4a), ilmenite-rich norites (~55% Fe–Ti oxides + ~40% Opx and plagioclase with minor Cpx; Fig. 4d) and ilmenite-rich melanorites (~40% Fe–Ti oxides + ~60% Opx, plagioclase with minor Cpx and amphibole; Fig. 4b, g). Plagioclase mostly occurs as prismatic crystals (1.0–3.0 mm) in semi-massive ores (Fig. 4a). Some plagioclase crystals form vermicular intergrowths with ilmenite, showing reactive symplectite textures (Fig. 4c). Pyroxenes occur as cumulus short idiomorphic prisms (0.2–1.0 mm), and exhibit thin reaction rims of amphiboles at contacts with ilmenite (Fig. 4b). They are sometimes partially to completely altered to tremolite, serpentine and talc (Fig. 4a–d). Amphibole occurs as large phenocrysts (1.0–2.5 mm), which are mostly corroded by hemo-ilmenite (Fig. 4d). It is also found as thin rims arround Fe–Ti oxide grains. Apatite occurs as fine idiomorphic inclusions in ilmenite (Fig. 4g).

The Abu Ghalaga Fe–Ti oxides are composed mainly of hemo-ilmenite (ilmenite with titanohematite lamellae) and ilmenite with minor titanomagnetite (Fig. 4c–h). Hemo-ilmenite is the main constituent of the Abu Ghalaga oxide ores and occurs as polygonal crystals (Fig. 4e, h). These crystals show 120° triple-junction contacts (Fig. 4e, h) and contain <50% exsolved titanohematite, showing magmatic origin (Fig. 4f–h). Hemo-ilmenite grains are mostly fresh, except in a few samples in which ilmenite was replaced by rutile (Fig. 4g). The exsolved titanohematite is found as irregular exsolution textures (Fig. 4f and g) in the host ilmenite (Fig. 4e–h). Ilmenite sometimes contains fine elongated lamellae of exsolved magnetite (Fig. 4f), which coexist with hematite exsolution lamellae within the same crystal.

Sulfide minerals are more abundant (3–5 vol%) in Abu Ghalaga ores (Fig. 4e–h) than in Korab Kansi ores. They occur either as fine inclusions in hemo-ilmenite grains (Fig. 4g) or as interstitial phases between hemo-ilmenite crystals and at their rims (Fig. 4e–h). They sometimes fill hemo-ilmenite cracks and fractures (Fig. 4h). The Abu Ghalaga sulfides are mainly pyrite with subordinate chalcopyrite, pyrrhotite and sphalerite, which crystallized with hemo-ilmenite (Fig. 4e–h). Pyrrhotite occurs mainly as inclusions (Fig. 4g) in ilmenite, but pyrite is the dominant interstitial phase (Fig. 4h).

## 5. Mineral chemistry

### 5.1. Major elements of minerals in Korab Kansi Fe–Ti–V ores

Olivines in Korab Kansi ores have chrysolite to hyalosiderite composition. They have narrow ranges of forsterite contents (Fo) from 68.8 to 74.2 mol%; olivines in Fe–Ti–V oxide-rich troctolites have lower Fo (69.8 mol%) than those (72.9 mol% Fo on average) of Fe–Ti–V oxide-rich dunites (Fig. 5a; Supplementary 2). The investigated olivines (Table 1; Supplementary 2) have similar NiO content (<0.05 wt%) and Fo to olivines in ferropicrites (Fig. 5a). Iddingsite has variable compositions according to the degree of olivine alteration.

Primary amphiboles in Korab Kansi Fe–Ti ores are pargasite (Leak

et al., 1997, Fig. 6c; Table 1; Supplementary 2), and have higher Mg# (0.7–1.0), $TiO_2$ (3.64 wt%), $Al_2O_3$ (14.22 wt%) and $Na_2O$ (3.17 wt% on average) than Abu Ghalaga primary amphiboles (Table 1; Supplementary 2). Plagioclase is labradorite ($An_{55.3-56.6}$) for Fe–Ti oxide-rich troctolites, and andesine to labradorite ($An_{48.9-56.6}$) for Fe–Ti–V oxide-rich dunites (Table 1; Supplementary 2). Spinel is aluminous (Cr#, 0.006) with a narrow range of $Al_2O_3$ (61.9–64 wt %), MgO (13.4–14.4 wt %) and FeO (21.5–23.5 wt %). Chlorite is ripidolite and clinochlore (Hey, 1954, Fig. 6e).

Magnetite-titanomagnetite solid solution has a wide range of ulvöspinel contents (0.6–72.5 mol%) (Stromer, 1983) (Table 2; Supplementary 3). Magnetite forms continuous solid solutions with ulvöspinel, forming titanomagnetite. There are two types of magnetite compositions: Ti-poor (0.2–2.7 wt% $TiO_2$) and Ti-rich (4.5–24.3 wt% $TiO_2$) (Fig. 6f; Supplementary 3). Ti-poor magnetite favors $Cr_2O_3$ relative to Ti-rich magnetite (Fig. 7f). In addition, $V_2O_5$ in magnetite exhibits a negative correlation with FeO (Fig. 8a). Magnetite FeO content varies from 67.4 to 89.9 wt% due to replacement by Ti, Mg, V and Mn (Fig. 7b–e). The Korab Kansi magnetite is poor in NiO, ZnO and CoO (<0.2 wt%), but rich in MnO (up to 1.4 wt%) (Supplementary 3).

The Korab Kansi ilmenite ranges widely in $X_{Ilm}$ [$Fe^{2+}$/($Fe^{2}$+$^{+}Fe^{3+}$+Mg+Mn)], from 0.79 to 0.98 and has a narrow range of FeO, 39.8–46.3 wt% (Fig. 6f, Supplementary 3). The ilmenite (mol% of Hem, 0.007 on average) is slightly higher in $TiO_2$ content (51.2–54.7 wt %) than that of Abu Ghalaga and Sept Iles ($TiO_2$, 48.6–50.6 wt%; Namur et al., 2010) layered intrusions (Fig. 8c). The Korab Kansi ilmenite has small amounts of $Cr_2O_3$ (<0.07 wt%), NiO (<0.03 wt%) and ZnO (<0.1 wt%), and exhibits a large variation of MgO content (0.05–3.0 wt%), similar to Panzhihua ilmenites (Fig. 8d). It is richer in $V_2O_5$ (3.1–3.8 wt %) and MnO (1.0 wt% on average) than coexisting titanomagnetite ($V_2O_5$, 1.2–2.0 wt% and MnO = 0.27 wt% on average; Fig. 8f). Elemental mapping of both magnetite and ilmenite for most elements shows homogeneous compositions from core to rim (Supplementary 6a-f). Sulfides in Fe–Ti oxide ores are mainly pyrrhotite and pyrite with subordinate chalcopyrite (Supplementary 4). They contain significant Mo (up to 0.8 wt%), Au (up to 0.3 wt%) and Ag (up to 0.33 wt%).

### 5.2. Major elements of minerals in Abu Ghalaga Fe–Ti ores

Pyroxenes in Abu Ghalaga ores have low concentrations of $TiO_2$, $Cr_2O_3$ and MnO (<0.5 wt%. The clinopyroxene (Cpx) is diopside ($Wo_{44.97-47.5}$) with a narrow range of Mg# (0.73–0.84) (Table 1; Supplementary 2; Fig. 5b), similar to Cpxs of Egyptian layered mafic-ultramafic intrusions (Khedr et al., 2020). The Abu Ghalaga Cpx contains less Ti and Al than Korab Kansi Cpx (Fig. 5c and d). Opx is enstatite ($En_{63.8-71.9}$) with a narrow range of Mg#, 0.65–0.76, similar to Opxs of ferrobasalts (Fig. 6a and b). It has wide ranges of $TiO_2$ (0.1–1.16 wt%), CaO (0.46–2.7 wt%), FeO (15.3–21.8 wt%) and $Al_2O_3$ (1.0–1.87 wt%) (Fig. 6a and b; Table 1; Supplementary 2).

Primary amphiboles in Fe–Ti ores are edenite with minor pargasite (Leak et al., 1997, Fig. 6c; Table 1). They have average contents of $TiO_2$ (1.6 wt%), $Al_2O_3$ (10.74 wt%), $Na_2O$ (1.5 wt%) and $K_2O$ (0.44 wt%) (Table 1; Supplementary 2). Secondary amphiboles are actinolite and magnesiohornblende for those replacing Cpx and are anthophyllite and gedrite for those replacing Opx (Supplementary 2; Fig. 6c and d). Plagioclase ranges from andesine to labradorite ($An_{44.4-55.5}$) (Table 1; Supplementary 2). Chlorite after Cpx or amphiboles is pycnochlorite, clinochlore and sheridanite (Fig. 6e).

The Abu Ghalaga titanomagnetite has a narow $TiO_2$ range (2.95–5.91 wt%), and contains minor $Al_2O_3$ (0.11–0.22 wt%), MgO (0.02–0.24 wt%), $Cr_2O_3$ (0.05–0.23 wt%) and MnO (<0.3 wt%) relative to that of the Korab Kansi (Table 2; Supplementary 3). The magnetite is of magmatic origin based on the Ni/Cr versus Ti diagram (Fig. 8b) (Dare et al., 2014). The Abu Ghalaga ilmenite shows higher FeO (44.97–50.95 wt%) and $Cr_2O_3$ (<0.12 wt%), but lower $TiO_2$ (45.3–50.18 wt%), MgO (0.06–3.1 wt%) and MnO (0.2–0.4 wt%) contents relative to those of the Korab Kansi due to abundance of exsolved hematite (Figs. 4 and 8e; Supplementary 3). It is ferrian type (8.7 mol% Hem, on average) with high $Fe_2O_3$ contents (6.1–13 wt%) than the Korab Kansi (0.1–6.5 wt%) (Fig. 6f; Supplementary 3). MgO is concentrated in ilmenite (1.8 wt% on average) relative to the exsolved titanohematite (0.3 wt%) (Supplementary 3). Titanohematite averages 67.8 wt% $Fe_2O_3$, 15.8 wt% $TiO_2$ and 13.6 wt% FeO (Table 2; Supplementary 3). Ilmenite major element mapping for Abu Ghalaga semi-massive and massive ores shows homogeneous compositions from core to rim (Supplementary 6g-i). Sulfides in Abu Ghalaga ores are mainly pyrite (with Au<0.14 wt%, Pt and Ir = 0.4 wt% on average) and chalcopyrite (with Au<0.14 wt%, Pt = 0.37 wt%) with subordinate pyrrhotite and sphalerite (with Pt = 1.15 wt %) (Supplementary 4).

### 5.3. Trace elements of minerals in Korab Kansi Fe–Ti–V ores

Trace-element contents of Korab Kansi olivines increase from fresh olivine (ΣREE = 0.2 ppm) to iddingsite ΣREE = 0.85 ppm) (Table 3). Chondrite (CI)-normalized REE patterns of olivine and iddingsite are spoon shaped with enrichment of light rare earth elements (LREE) relative to heavy rare earth elements (HREE) $(La/Yb)_N$ = 2.37–12.64 (Fig. 9a). Olivine multi elemental patterns show positive anomalies for fluid-mobile elements (e.g., Pb, Ba, Sr, Rb, U) and Ni, but exhibit negative anomalies for Nb, Nd, Co, Th and V (Fig. 9b).

REE patterns of Korab Kansi amphiboles in Fe–Ti–V oxide-rich dunites are nearly flat (La/Lu)N = 1.01–1.34, while those in Fe–Ti–V oxide-rich troctolites are nearly U-shaped (Fig. 9g). Multi elemental patterns of amphiboles are mostly enriched in large ion lithophile elements (LILE; e.g. Rb, Ba and Sr), U, La, Ce, Pr and Nd (>2 times PM) and depleted in Co, Cr and Ni (Fig. 9h). REE patterns of plagioclase show pronounced Eu positive anomalies and are enriched in LREE relative to HREE (Fig. 9i). Multi elemental patterns of plagioclase in Fe–Ti–V oxide-rich dunites are enriched in most trace elements relative to plagioclase of Fe–Ti–V oxide-rich troctolites (Fig. 9j). The CI-normalized REEs of ilmenites exhibit U-shaped patterns with slightly enriched HREE relative to LREE (Fig. 10a). Ilmenite multi elemental patterns show strong positive anomalies for high field strength elements (HFSE: Nb, Ta, Zr, Hf) and V, but negative anomalies for Li, Cs, Rb, Ba, and LREE (Fig. 10b). The Korab Kansi magnetite-titanomagnetite shows wide ranges of V (7842–10251 ppm), Co (48.6–199 ppm), Zn (31–277 ppm) and Ga (16.5–75.2 ppm). It is poor in REE (ΣREE, up to 0.25 ppm) contents (Fig. 10c) relative to REE (ΣREE, up to 0.73 ppm) of ilmenite (Table 3; Supplementary 5).

### 5.4. Trace elements of minerals in Abu Ghalaga Fe–Ti ores

CI-normalized REE patterns of Cpx in Abu Ghalaga ores are convex upward with negative Eu anomalies, similar to Cpx REE patterns of Fe–Ti–V oxide-bearing troctolites from the Sept Iles layered intrusion in Canada (Namur et al., 2011) and Motaghairat layered anorthosites from the SED (Fig. 1a) of Egypt (Ab del Halim et al., 2016) (Fig. 9c). Primitive mantle (PM)-normalized Cpx patterns show negative anomalies for Pb, Sr, Nb, Ta, Zr, Hf, Eu, Cr and Ni (Fig. 9d). The depletion of Eu and Sr in Cpx suggests that the magma experienced significant plagioclase fractionation. REE patterns of Abu Ghalaga Opx are steeply inclined with LREE depletion relative to HREE $(La/Yb)_N$ = 0.04–0.36), and exhibit

**Table 3**
Representative trace and rare earth elements (ppm) of silicates and Fe–Ti oxides in Korab Kansi and Abu Ghalaga ore layers.

| Area | | | | Abu Ghalaga | | | | | Korab Kansi | | |
|---|---|---|---|---|---|---|---|---|---|---|---|
| Rock type | Fe–Ti–V oxide-rich Dunite | | | Ilmenite melanorite | | | Ilmenitite | | Fe–Ti–V oxide-rich troctolite | Fe–Ti–V oxide-rich Dunite | |
| Mineral | olivine | Altered Olivine | Iddingsite | Clinoenstatite | | | Diopside | | Pargasite | | |
| Sample | Kn.23 | Kn.10 | Kn.10 | Ghl.23 | | | Ghl.42 | Ghl.35 | Kn-16 | Kn-10 | Kn-23 |
| Trace elements (ppm) | | | | | | | | | | | |
| Li | 0.22 | 0.14 | 0.39 | 1.02 | 1.29 | 7.17 | 6.18 | 7.29 | 4.09 | 7.75 | 2.86 |
| B | 0.08 | 0.02 | 0.04 | 0.07 | 0.13 | 0.21 | 0.85 | 0.34 | 0.40 | 0.90 | 0.32 |
| Sc | 0.16 | 0.06 | 0.13 | 19.26 | 25.79 | 101.14 | 162.04 | 145.07 | 102.09 | 228.57 | 131.09 |
| Ti | 10.76 | 5.63 | 13.88 | 764.3 | 1582.4 | 3332.9 | 5608.4 | 4102.1 | 20306 | 25419 | 23577 |
| V | 0.21 | 0.14 | 0.30 | 51.94 | 70.88 | 280.31 | 372.73 | 370.69 | 609.01 | 719.66 | 642.06 |
| Cr | – | – | – | 15.25 | 22.84 | 72.57 | 97.60 | 151.53 | – | – | – |
| Co | 4.04 | 1.07 | 0.45 | 51.78 | 67.60 | 59.91 | 75.17 | 46.06 | 59.59 | 85.52 | 55.09 |
| Ni | – | – | – | 40.71 | 55.91 | 65.45 | 180.93 | 91.11 | – | – | – |
| Zn | 1.12 | 0.20 | 0.64 | 131.36 | 157.09 | 86.72 | 79.39 | 40.10 | 41.35 | 90.93 | 41.77 |
| Ga | 0.05 | 0.06 | 0.16 | 4.05 | 5.06 | 9.79 | 30.40 | 15.21 | 12.91 | 11.84 | 12.20 |
| Rb | 1.01 | 1.11 | 3.49 | Bdl | 0.90 | 1.66 | 1.78 | 0.20 | 1.94 | 2.91 | 3.31 |
| Sr | 2.20 | 2.52 | 8.38 | 0.07 | 2.06 | 24.3 | 20.0 | 16.6 | 279.2 | 153.6 | 171.0 |
| Sr | 2.36 | 2.59 | 8.28 | 0.14 | 1.89 | 23.4 | 21.4 | 18.9 | 273.1 | 159.5 | 173.4 |
| Y | 0.04 | 0.05 | 0.14 | 4.09 | 9.27 | 57.18 | 91.34 | 74.64 | 16.70 | 61.95 | 22.19 |
| Zr | 1.14 | 0.91 | 2.60 | 1.92 | 4.92 | 41.50 | 41.88 | 50.60 | 47.08 | 90.94 | 48.79 |
| Nb | 0.02 | 0.02 | 0.06 | 0.00 | 0.15 | 0.18 | 0.63 | 0.83 | 1.52 | 2.85 | 2.37 |
| Cs | 0.01 | 0.01 | 0.02 | 0.00 | 0.04 | 0.05 | 0.25 | 0.00 | 0.06 | 0.06 | 0.05 |
| Ba | 7.87 | 6.66 | 21.05 | 0.02 | 4.43 | 8.21 | 7.54 | 8.90 | 3.0 | 75.7 | 72.3 |
| La | 0.05 | 0.07 | 0.20 | 0.04 | 0.34 | 6.54 | 3.71 | 5.78 | 2.70 | 11.32 | 5.40 |
| Ce | 0.07 | 0.12 | 0.36 | 0.15 | 1.29 | 29.54 | 19.35 | 21.86 | 10.43 | 32.82 | 14.40 |
| Pr | 0.01 | 0.01 | 0.04 | 0.03 | 0.25 | 5.83 | 5.21 | 5.02 | 1.91 | 5.49 | 2.13 |
| Nd | 0.03 | 0.04 | 0.13 | 0.27 | 1.51 | 34.67 | 38.45 | 33.26 | 10.44 | 29.51 | 9.63 |
| Sm | 0.01 | 0.01 | 0.02 | 0.16 | 0.70 | 11.82 | 17.93 | 13.06 | 2.71 | 8.95 | 2.34 |
| Eu | 0.00 | 0.01 | 0.01 | 0.04 | 0.11 | 2.48 | 2.92 | 2.65 | 1.56 | 3.04 | 1.61 |
| Gd | 0.00 | 0.01 | 0.02 | 0.38 | 1.10 | 13.92 | 21.49 | 16.97 | 2.53 | 10.40 | 3.28 |
| Tb | 0.01 | 0.00 | 0.00 | 0.07 | 0.19 | 2.14 | 3.40 | 2.79 | 0.42 | 1.87 | 0.54 |
| Dy | 0.00 | 0.00 | 0.02 | 0.67 | 1.49 | 13.03 | 20.36 | 17.99 | 2.91 | 11.28 | 3.59 |
| Ho | 0.00 | 0.00 | 0.01 | 0.15 | 0.38 | 2.23 | 3.60 | 3.54 | 0.62 | 2.35 | 0.78 |
| Er | 0.00 | 0.01 | 0.01 | 0.57 | 1.03 | 5.38 | 8.43 | 8.22 | 1.89 | 6.66 | 2.62 |
| Tm | 0.01 | 0.01 | 0.00 | 0.09 | 0.19 | 0.69 | 0.88 | 1.03 | 0.34 | 0.96 | 0.42 |
| Yb | 0.01 | 0.00 | 0.01 | 0.65 | 1.14 | 4.17 | 4.61 | 5.31 | 2.52 | 6.44 | 3.33 |
| Lu | 0.00 | 0.00 | 0.00 | 0.11 | 0.18 | 0.57 | 0.58 | 0.73 | 0.39 | 0.89 | 0.57 |
| Hf | 0.03 | 0.03 | 0.08 | 0.08 | 0.26 | 1.60 | 2.33 | 2.66 | 1.64 | 3.45 | 1.60 |
| Ta | 0.00 | 0.00 | 0.00 | Bdl | 0.02 | 0.02 | 0.04 | 0.05 | 0.09 | 0.19 | 0.11 |
| Pb | 0.11 | 0.14 | 0.54 | 0.00 | 0.01 | 0.23 | 0.13 | 0.18 | 0.31 | 1.72 | 1.00 |
| Th | 0.02 | 0.02 | 0.04 | 0.01 | 0.06 | 0.31 | 0.19 | 0.06 | 0.25 | 0.46 | 0.18 |
| U | 0.01 | 0.02 | 0.06 | 0.00 | 0.01 | 0.04 | 0.03 | 0.07 | 0.06 | 0.14 | 0.04 |
| ΣREE | 0.20 | 0.28 | 0.84 | 3.38 | 9.91 | 133.01 | 150.91 | 138.21 | 41.37 | 132.00 | 50.63 |
| (La/Lu)N | 1.60 | 6.16 | 13.88 | 0.03 | 0.20 | 1.20 | 0.67 | 0.82 | 0.72 | 1.32 | 0.98 |
| (La/Yb)N | 5.16 | 14.95 | 10.74 | 0.04 | 0.20 | 1.07 | 0.55 | 0.74 | 0.73 | 1.19 | 1.10 |

(–): not analyzed.
bdl: below detection limits.

pronounced Eu anomalies (Fig. 9e). They show similar patterns to Opx from Motaghairat anorthosites (Fig. 9e). The PM-normalized trace-element patterns of Opx are depleted in Pb, Sr, Eu, Ta, Cr and Ni (Fig. 9f).

REE patterns of Abu Ghalaga amphiboles differ from those of the Korab Kansi, and show a convex-upward shape with LREE depletion (La/Yb = 0.42–1.0; Fig. 9g). Trace-element contents of Abu Ghalaga amphiboles are higher than those in the Korab Kansi with some enrichment of HFSE (e.g. Nb, Ta) and depletion of LILE (e.g. Cs, Rb, Sr and Pb), Th and U (Fig. 9h). The Abu Ghalaga plagioclase REE values and patterns resemble those of Korab Kansi gabbros, displaying steeply inclined patterns from La to Yb (Fig. 9i).

The CI-normalized REEs of Abu Ghalaga ilmenites display U-shaped patterns (Fig. 10a). Abu Ghalaga ilmenite has higher $(La/Lu)_N$ ratio (0.55–0.81) than that of the Korab Kansi [$(La/Lu)_N$ = 0.01–0.12]. The Abu Ghalaga ilmenite is slightly enriched in Li, Nb, Ta, Ga and LREE, relative to Korab Kansi ilmenite (Fig. 10b). CI-normalized REEs of the Abu Ghalaga titanohematite display U-shaped patterns (Fig. 10c; Table 3; Supplementary 5). The multi elemental patterns of this titanohematite show a strong positive anomaly for HFSE (e.g. Nb, Ta, Zr and Hf) and V, while Ba shows a strong negative anomaly (Fig. 10c).

## 6. Discussion

### 6.1. Subsolidus modification of SED Fe–Ti–V ore deposits

The investigated titanomagnetites sometimes suffer from subsolidus re-equilibration with ilmenite due to $Fe^{2+}$-Mg redistribution during slow cooling (e.g., Charlier et al., 2007), causing enrichment of Mg in

| Abu Ghalaga | | Korab Kansi | | | Korab Kansi | | | Abu Ghalaga | | | | |
|---|---|---|---|---|---|---|---|---|---|---|---|---|
| Ilmenitite | | Fe–Ti–V oxide-rich troctolite | Fe–Ti–V oxide-rich Dunite | Ilmenitite | Fe–Ti–V oxide-rich Dunite | Fe–Ti–V oxide-rich Dunite | | Fe–Ti–V oxide-rich Dunite | Ilmenite melanorite | | Ilmenitite | |
| Edenite | Actinolite | Labradorite | | | Magnetite | Ti-magnetite | | Ilmenite | | | Hematite | |
| Ghl.23 | Ghl.35 | Kn-16 | Kn-23 | Ghl.42 | Kn.23 | Kn.16 | Kn.10 | Kn.10 | Ghl.23 | Ghl.35 | Ghl.42 | Ghl.42 |
| 1.63 | 2.85 | 0.15 | bdl | 0.12 | 0.00 | 1.46 | 0.05 | 0.02 | 0.51 | 1.21 | 0.23 | 0.23 |
| 0.16 | 0.12 | 0.18 | 1.32 | 0.25 | 0.01 | 0.44 | 0.10 | 0.10 | 0.08 | 0.07 | 0.03 | 0.02 |
| 110.31 | 110.60 | 0.83 | 1.47 | 0.88 | 1.15 | 2.14 | 7.44 | 55.17 | 60.54 | 59.05 | 18.69 | 13.43 |
| 12446 | 56973 | 208.7 | 501.5 | 384.6 | – | – | – | – | – | – | – | – |
| 474.02 | 596.36 | 4.28 | 4.91 | 0.63 | 7842.3 | 8906.6 | 10251.0 | 20600.2 | 1849.9 | 1772.1 | 487.1 | 374.1 |
| 126.77 | 209.81 | – | – | – | – | – | – | – | – | – | 95.18 | 69.61 |
| 72.35 | 40.09 | 0.43 | 8.56 | 0.06 | 22.62 | 81.62 | 88.91 | 85.83 | 30.29 | 30.37 | 23.02 | 14.58 |
| 110.98 | 74.68 | – | – | – | – | – | – | – | – | – | 9.25 | 5.84 |
| 93.70 | 59.93 | 0.18 | 17.46 | 0.73 | 14.76 | 124.69 | 149.76 | 5.79 | 69.03 | 45.58 | 9.34 | 10.98 |
| 21.16 | 14.76 | 19.94 | 10.41 | 28.92 | 7.27 | 28.99 | 24.26 | 0.61 | 5.92 | 4.50 | 1.38 | 1.21 |
| 1.21 | 0.24 | 0.03 | 25.76 | 0.08 | 0.00 | 0.04 | 0.01 | 0.02 | 0.01 | 0.03 | 0.00 | 0.01 |
| 75.6 | 15.5 | 1056.8 | 1055.5 | 791.1 | bdl | 2.28 | 0.14 | 0.55 | bdl | bdl | bdl | bdl |
| 72.1 | 15.6 | 1231.5 | 1245.3 | 791.5 | 0.03 | 1.81 | 0.19 | 0.77 | 0.63 | 0.65 | 0.26 | 0.13 |
| 129.71 | 60.07 | bdl | 1.16 | 0.36 | 0.00 | 0.00 | 0.11 | 0.11 | 0.20 | 0.10 | 0.03 | 0.02 |
| 64.95 | 39.99 | 0.02 | 27.02 | 0.09 | 0.47 | 1.63 | 3.44 | 92.40 | 19.64 | 26.08 | 6.75 | 4.71 |
| 4.91 | 17.23 | bdl | 0.55 | 0.02 | 0.00 | 0.01 | 0.02 | 8.14 | 72.55 | 62.39 | 18.49 | 13.00 |
| 0.00 | 0.01 | 0.00 | 0.44 | bdl | bdl | 0.00 | bdl | bdl | bdl | bdl | bdl | bdl |
| 56.5 | 10.7 | 2.2 | 340.3 | 113.7 | 0.02 | 0.01 | 0.05 | 0.31 | bdl | 0.04 | 0.00 | 0.00 |
| 13.96 | 2.99 | 1.42 | 2.18 | 2.90 | 0.00 | 0.00 | 0.03 | 0.01 | 0.08 | 0.05 | 0.02 | 0.01 |
| 61.29 | 13.68 | 2.14 | 3.81 | 7.33 | 0.00 | 0.02 | 0.07 | 0.01 | 0.21 | 0.17 | 0.05 | 0.02 |
| 11.64 | 3.33 | 0.15 | 0.49 | 0.64 | bdl | 0.00 | 0.01 | bdl | 0.02 | 0.01 | 0.01 | 0.00 |
| 66.13 | 23.88 | 0.66 | 1.51 | 2.38 | bdl | 0.01 | 0.05 | 0.00 | 0.09 | 0.08 | 0.03 | 0.02 |
| 21.51 | 10.32 | 0.02 | 0.15 | 0.37 | 0.00 | 0.03 | 0.04 | bdl | 0.04 | 0.00 | 0.01 | 0.00 |
| 4.99 | 2.17 | 0.26 | 0.40 | 1.61 | bdl | 0.01 | 0.00 | bdl | 0.01 | 0.00 | 0.00 | 0.00 |
| 24.94 | 13.23 | bdl | 0.13 | 0.19 | bdl | bdl | bdl | bdl | bdl | 0.03 | 0.00 | 0.00 |
| 4.04 | 2.07 | 0.02 | 0.02 | 0.03 | bdl | bdl | bdl | 0.00 | 0.00 | 0.01 | 0.00 | 0.00 |
| 26.63 | 13.80 | 0.01 | 0.20 | 0.13 | 0.00 | 0.00 | 0.02 | bdl | 0.03 | 0.01 | 0.01 | 0.00 |
| 5.04 | 2.61 | 0.00 | 0.03 | 0.01 | bdl | 0.00 | 0.01 | bdl | 0.00 | 0.01 | 0.00 | 0.00 |
| 12.50 | 6.64 | 0.00 | 0.09 | 0.02 | bdl | bdl | 0.01 | 0.05 | 0.02 | 0.03 | 0.00 | 0.00 |
| 1.57 | 0.86 | 0.00 | 0.01 | 0.00 | 0.00 | bdl | 0.01 | 0.02 | 0.01 | 0.00 | 0.00 | 0.00 |
| 8.98 | 4.83 | bdl | 0.10 | bdl | bdl | 0.03 | 0.01 | 0.17 | 0.03 | 0.03 | 0.02 | 0.01 |
| 1.09 | 0.54 | 0.01 | 0.02 | 0.00 | bdl | 0.00 | 0.00 | 0.07 | 0.02 | 0.01 | 0.00 | 0.00 |
| 3.04 | 3.14 | bdl | 0.62 | bdl | 0.02 | 0.06 | 0.15 | 2.25 | 2.50 | 3.72 | 0.97 | 0.71 |
| 0.25 | 1.55 | bdl | 0.05 | 0.00 | 0.00 | bdl | 0.00 | 0.72 | 5.57 | 5.72 | 1.67 | 1.22 |
| 0.36 | 0.05 | 0.78 | 3.72 | 2.51 | 0.00 | 0.01 | 0.01 | 0.00 | 0.00 | 0.01 | 0.00 | 0.00 |
| 0.08 | 0.01 | bdl | 0.33 | 0.01 | 0.00 | 0.00 | 0.00 | 0.00 | bdl | 0.01 | 0.01 | 0.00 |
| 0.01 | 0.00 | 0.00 | 0.39 | 0.00 | 0.00 | bdl | bdl | 0.01 | 0.01 | 0.01 | 0.00 | 0.00 |
| 264.31 | 100.96 | 4.70 | 9.14 | 15.61 | 0.01 | 0.11 | 0.25 | 0.33 | 0.56 | 0.45 | 0.15 | 0.09 |
| 1.33 | 0.57 | 17.76 | 11.08 | 120.27 | 0.00 | 0.16 | 3.70 | 0.01 | 0.55 | 0.68 | 0.34 | 0.07 |
| 1.06 | 0.42 | 0.00 | 15.17 | 0.00 | 0.00 | 0.07 | 2.64 | 0.03 | 2.05 | 1.12 | 0.67 | 0.10 |

ilmenite relative to magnetite (Supplementary 3). The MgO content in SED ilmenite ranges from 0.05 to 3.0 wt% (Supplementary 3), and the ilmenite in contact with ferromagnesian silicates has high MgO content, reflecting postcumulus re-equilibration with these silicates and $Fe^{2+}$-Mg exchange. During subsolidus cooling, magnetite loses Al, Mg and Ti by exsolving Al-spinel and ilmenite lamellae (Fig. 3).

Ilmenite easily recrystallizes under subsolidus conditions, meaning that cations effectively diffuse (Charlier et al., 2015). The following features support recrystallization of Abu Ghalaga Fe–Ti oxide deposits: 1) dominance of annealing texture (granoblastic) of hemo-ilmenite, which indicates static recrystallization (Fig. 4e, h); 2) occurrence of twinning, displacement and folding of hematite exsolution lamellae (Fig. 4g); and 3) existence of intergranular films of hematite or magnetite along hemo-ilmenite borders due to migration of $Fe_2O_3$ from inside the crystal to the rims due to subsolidus modification (Fig. 4g).

### 6.2. Implications of SED Fe–Ti–V oxide textures

Oxide intergrowths reflect many factors operating during crystallization of Fe–Ti oxide deposits such as oxygen fugacity, temperature, and chemical conditions of the parent melts (Tan et al., 2016). Ilmenite is generated either by direct crystallization from parent melts, or as a product of oxidation-exsolution from titanomagnetite (Frost and Lindsley, 1991). The Korab Kansi titanomagnetite (Fig. 3; Supplementary 3) generally has (111) oxidation-exsolution lamellae of ilmenite, forming ilmenite-titanomagnetite intergrowths (Fig. 3e–h). Interstitial titanomagnetite between cumulus olivines (Fig. 3) includes oxy-exsolution of ilmenite and spinel lamellae (Fig. 3g and h). This occurrence suggests formation of ilmenite as a result of oxidation-exsolution of titanomagnetite (e.g., Frost and Lindsley, 1991; Liu et al., 2015), and a magmatic origin of both minerals. Ilmenite granules and trellis-type lamellae (Fig. 3g and h) in titanomagnetite may

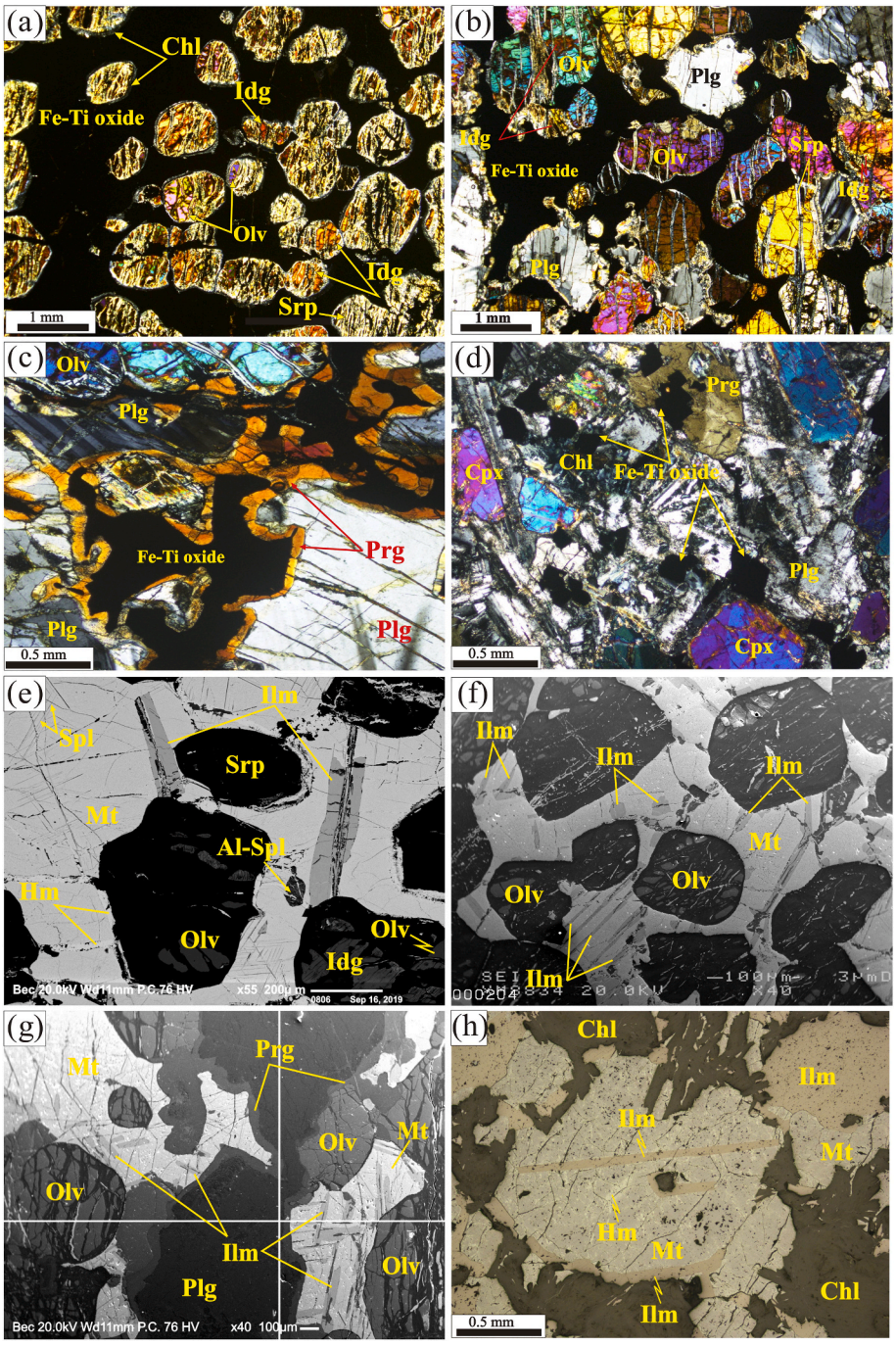


**Fig. 3.** Photomicrographs of Fe–Ti–V oxide ores in the Korab Kansi mafic-ultramafic intrusion. All photos are back-scattered electron images, except **a-d** taken under crossed polarized light and **h** taken under reflected light. **a**) Net-textured Fe–Ti oxides between cumulus olivine (Olv) crystals, showing cumulate texture. This olivine is highly altered to iddingsite (Idg) in semi-massive ore hosted in dunites. **b**) Cumulus crystals of olivine (Olv) and plagioclase (Plg) thermally corroded and invaded by intercumulus Fe–Ti–V oxide minerals in disseminated ores hosted by troctolites. **c**) Thin rim of brown hornblende (pargasite; Prg) occurring at the Fe–Ti oxide ore and plagioclase interface suggesting reaction between both of them in disseminated ores hosted by troctolites. **d**) Chadacrysts of Fe–Ti oxides included in plagioclase (Plg), clinopyroxene (Cpx) and pargasite (Prg); plagioclase sometimes shows zoning. **e**) Ilmenite-titanomagnetite sandwich intergrowth with very fine Al-spinel (Spl) exsolution lamellae or granules in semi-massive ores. **f**) Net-textured interstital titanomagnetite grains including (111) oxidation-exsolution ilmenite lamellae. **g**) Exsolution trellis texture of ilmenite in magnetite that enveloped by thin pargasite rim at the contact with plagioclase in disseminated ores in troctolites. **h**) The different occurrences of ilmenite as sandwich lamellae and composite intergrowths with magnetite that was pitted by hematite (Hm) in massive ores.

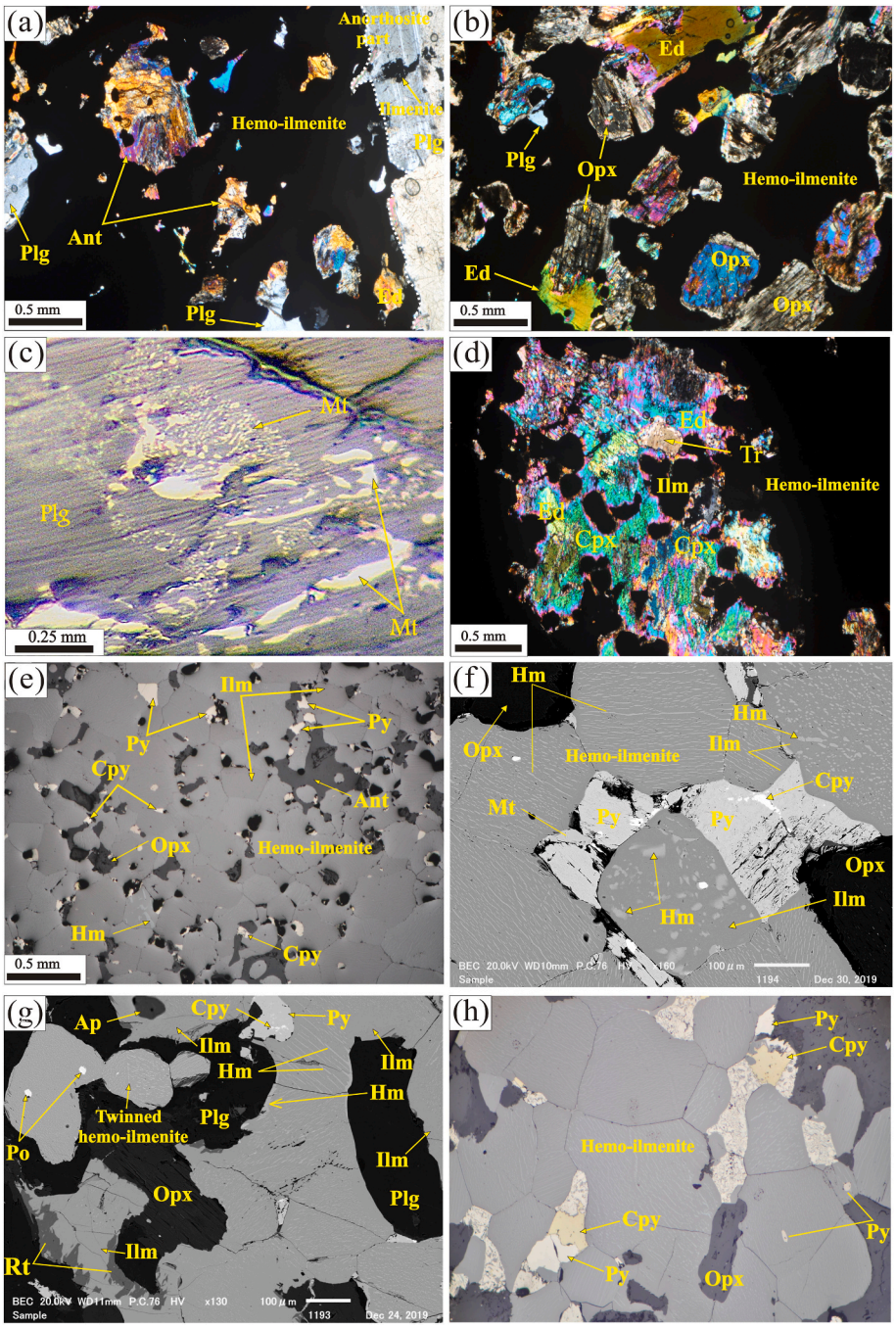


**Fig. 4.** Photomicrographs of Fe–Ti–V oxide ores in the Abu Ghalaga mafic intrusion. All photos were taken using Scanning Electron Microscope (SEM), except **a, b** taken using crossed polarized light and **c** as well as **e** taken under reflected light. **a**) Irregular contact between the hemo-ilmenite ore pitted with anthophyllite (Ant) and the host anorthosites. **b**) Idiomorphic primocrysts of orthopyroxene (Opx) and edenite (Ed) surrounded by interstitial net-textured hemo-ilmenite in ilmenite-rich melanorites. **c**) Symplectite texture formed due to ilmenite intergrowth with plagioclase as evidence of liquid immiscibilty, showing vermicular or wormy-like plagioclase in the host anorthosites. **d**) Dendritic oikocrysts of edenite (Ed) and clinopyroxene (Cpx) enclosing cumulates or chadacrysts of Fe–Ti oxides. Large intercumulus ilmenite showing amoeboidal texture and sending offshoots into clinopyroxene (Cpx) and edenite that is altered to tremolite (Tr). **e**) Polygonal ilmenite and hemo-ilmenite with 120° triple junction boundaries and pitted by pyrite (Py), chalcopyrite (Cpy), Opx and anthophyllite (Ant) in ilmenitite. **f**) Intercumulus sulfides filling spaces between the hemo-ilmenite that showing two different generations of hematite (Hm)-ilmenite (Ilm) intergrowth with intercumulus pyrite (Py) in ilmenite-melanorites. Ilmenite (grey) includes very fine Ti-hematite exsolution lamellae (light color). **g**) Twinned hemo-ilmenite crystals and cumulus apatite (Ap) with intercumulus sulfides (Py, Po), where hemo-ilmenite replaced by thin rims of titanohematite and late-magmatic rutile in ilmenite-melanorites. **h**) Interlocked hemo-ilmenite grains showing 120° triple junction boundaries with interstitial sulfides (Py, Cpy) in ilmenite-melanorites. Ilmenite has multiple generations of titanohematite exsolution lamellae, mainly parallel to (0001).

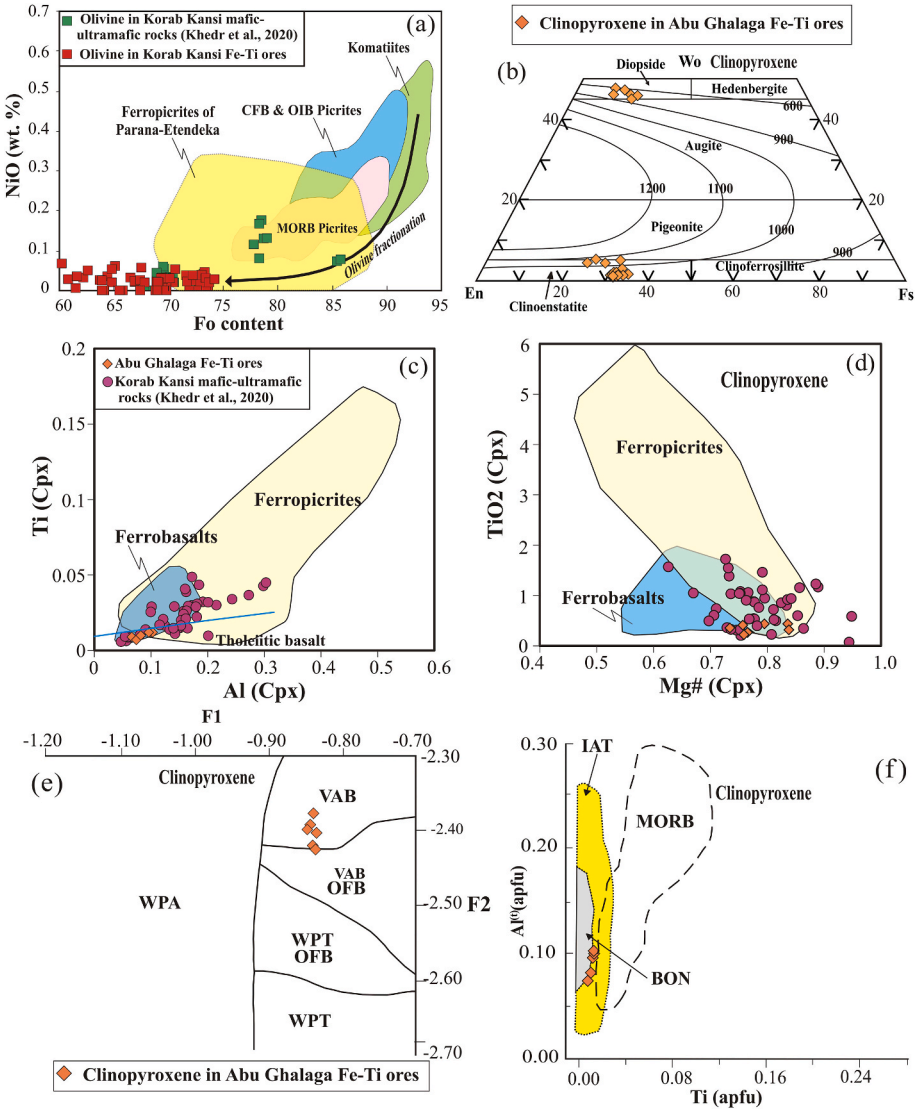


**Fig. 5.** Mineral chemistry of silicates in SED Fe–Ti–V oxide ores. **a**) Fo content versus NiO (wt%) for olivines in Korab Kansi oxide ores and host rocks. Fields of Parana'–Etendeka ferropicrites, worldwide komatiites, CFB and OIB picrites and MORB picrites as well as olivine fractionation trend are after Tuff et al. (2005). **b**) Wo-En-Fs diagram of Abu Ghalaga clinopyroxene (Cpx) compositions (Morimoto et al., 1988) with isothermal lines after Lindsley (1983). **c**) Cations of Al (total) vs. Ti for Abu Ghalaga Cpx (Leterrier et al., 1982). **d**) Mg# vs. $TiO_2$ for Cpx. Ferropicrite Cpx data (c, d) are compiled from Gibson et al. (2000), Tuff et al. (2005) and Desta et al. (2014), while ferrobasalt Cpx data are compiled from Lustrino (2006) and Namur et al. (2012). **e**) F1 vs. F2 diagram for Abu Ghalaga Cpx from basic lavas of magma types; $F_1$ (= −0.012 x $SiO_2$ - 0.0807 x $TiO_2$ + 0.0026 x $A1_2O_3$ - 0.0012 x FeO* - 0.0026 x MnO + 0.0087 x MgO - 0.0128 x CaO - 0.0419 x $Na_2O$) and $F_2$ (= −0.0469 x $SiO_2$ -0.0818 x $TiO_2$ -0.0212 x $A1_2O_3$ -0.0041 x FeO*-0.1435 x MnO - 0.0029 x MgO + 0.0085 x CaO + 0.0160 x $Na_2O$), where VAB: volcanic arc basalts, OFB: ocean-floor basalts, WPT: within plate tholeiitic basalts and WPA: within plate alkalic basalts are after Nisbet and Pearce (1977). **f**) Cations of Ti against $Al^{(t)}$ of Abu Ghalaga Cpx, where island-arc tholeiites (IAT), mid-ocean ridge basalts (MORB) and boninites (BON) fields are after Beccaluva et al. (1989).

result from oxidation of ulvöspinel above the magnetite–ulvöspinel solvus during subsolidus cooling (Charlier et al., 2015). Thus, our ilmenite-magnetite intergrowths (Fig. 3g and h) may be attributed to direct exsolution or "oxy-exsolution'' at a broad range of temperatures, and possibly indicate variations in the oxidation and cooling history of the layered intrusion (Buddington and Lindsley, 1964; Haggerty, 1991). During slow cooling, titanium in Korab Kansi titanomagnetite or magnetite-ilmenite solid solution may exsolve to form either discrete lamellae of ilmenite in magnetite (Fig. 3g and h) or granular exsolutions (Fig. 3g and h) of ilmenite around magnetite grains during oxy-exsolution. The Korab Kansi titanomagnetite includes Al-spinel exsolution lamellae or granules (Fig. 3e), and contains significant amount of $Al_2O_3$ (up to 3.7 wt%; Supplementary 3). Aluminous spinel exsolution (Fig. 3e) is due to the low solubility of $Al_2O_3$ in magnetite (Fig. 7a) during slow cooling (Charlier et al., 2010, 2015), and reflects significant amounts of Al in primary melts.

On the other hand, the Abu Ghalaga hemo-ilmenite occurs as cumulate and polygonal crystals with triple junction boundaries (120° intersections), suggesting a magmatic origin (Fig. 4g–h). It has abundant hematite exsolution lamellae parallel to (0001), forming hemo-ilmenite exsolution texture (Fig. 4f–g). This texture is interpreted to reflect unmixing of hematite-ilmenite solid solution during slow cooling (Ramdohr, 1980), and possibly formed in the late magmatic stage. The exsolved titanohematite is found as irregular exsolution plebs (Fig. 4f and g), spots, and threads or needle shapes parallel to the (0001) direction of the host ilmenite (Fig. 4e–h). The different shapes and orientations of titanohematite exsolution may indicate more than one generation. The high hematite content in ilmenite (6–13 mol%; Supplementary 3) and high $fO_2$ of the parent melts are responsible for generating this intergrowth (Fig. 4f–h), similar to Adirondacks hemo-ilmenite in New York (Basley and Buddington, 1958). Ilmenite may alter to rutile in Abu Ghalaga ores (Fig. 4g) under strongly oxidizing conditions (Frost and Lindsley, 1991), and some ilmenite rims around hemo-ilmenite are free of hematite exsolution (Fig. 4g) due to diffusional loss of $Fe^{3+}$ at the grain boundary.

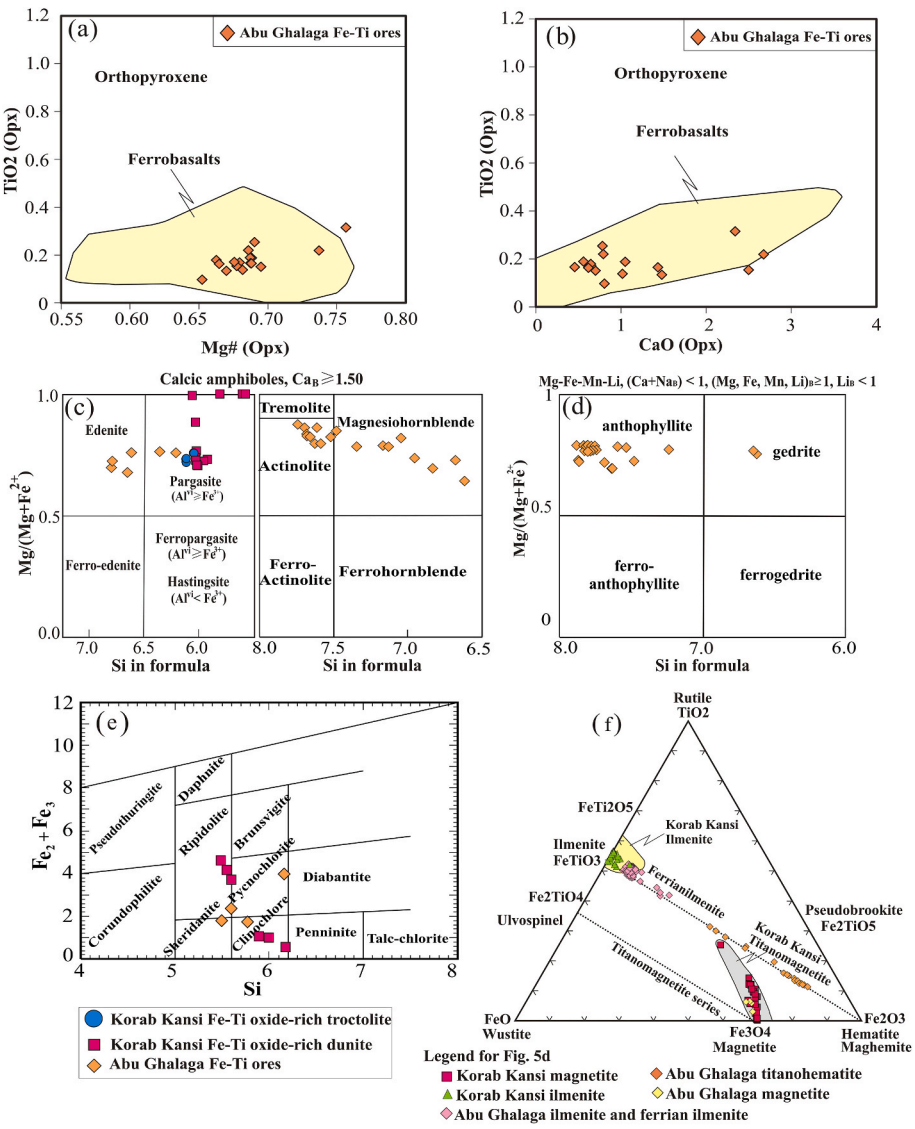


**Fig. 6.** Chemistry of Abu Ghalaga and Korab Kansi silicates. **a)** Mg# vs. $TiO_2$ for Opx. **b**) CaO vs. $TiO_2$ for Opx. Ferrobasalt Opx data (**a, b**) are compiled from Morisset (2008), Charlier et al. (2010) and Namur et al. (2012). **c, d**) Nomenclature diagrams for amphiboles coexisting with the Fe–Ti oxide ores (Leake et al., 1997). **e)** Si vs. $Fe^{+2} + Fe^{+3}$ for the SED chlorite associating oxide ores (Hey, 1954). **f**) $FeO–TiO_2–Fe_2O_3$ triangular classification diagram of Fe–Ti oxides (Buddington and Lindsley, 1964), showing the composition of Abu Ghalaga and Korab Kansi magnetite, hematite and ilmenite from the Fe–Ti oxide ore layers. Yellow and grey fields of Fe–Ti oxide minerals hosted in Korab Kansi mafic-ultramafic rocks are used for comparison (Khedr et al., 2020).

### 6.3. T-P- $f_{O2}$ conditions of SED Fe–Ti–V ore deposits

The abundance of titanomagnetite over ilmenite (Fig. 3e–h) in Korab Kansi Fe–Ti–V oxide ores can be explained by low Ti content in the primary melts. However Ti-rich melts may reach ilmenite saturation before magnetite crystallization, even in oxidizing conditions, and in some cases may crystallize hemo-ilmenite without magnetite (Lattard et al., 2005), like Abu Ghalaga hemo-ilmenite (Fig. 4e–h) formed under high $f_{O2}$ of Ti-rich parent melts. This is similar to the case for hemo-ilmenite in the Grader layered intrusion (Charlier et al., 2008, Fig. 8), where high hematite content in ilmenite indicates the high $f_{O2}$ of the Ti-rich parent melts. Abu Ghalaga hemo-ilmenite deposits require both high $TiO_2$ content of the parental magma and more oxidizing conditions.

Crystallization temperature ($T$) of Abu Ghalaga Opx in Fe–Ti ores and host gabbroic rocks based on projection of isothermal lines (Lindsley, 1983) ranges from 900 to 1100 °C (Fig. 5b). This temperature agrees with that calculated after Brey and Kohler (1990) based on Ca content of Opx, which yields 1082 °C for ilmentites and 1010 °C for ilmenite-rich melanorites. Abu Ghalaga Opx temperature is lower than that of Korab Kansi Opx in olivine gabbros (~1180 °C) and gabbronorites (~1116 °C). This crystallization temperature is higher than the equilibrium subsolidus temperature calculated based on pyroxene pairs. Three Opx and Cpx pairs from Abu Ghalaga ilmenitites, ilmenite-rich norites and ilmenite-rich melanorites reveal equilibration temperatures (Brey and Kohler, 1990) of 811 °C, 750 °C and 780 °C on average, respectively. These subsolidus temperatures (~750–900 °C) of Abu Ghalaga rocks are lower than those of Korab Kansi gabbroic rocks based on Opx and Cpx thermometry equations after Brey and Kohler (1990), which yield 820–997 °C (Khedr et al., 2020).

Equilibrium between ilmenite and magnetite has been used widely for estimating both temperatures and oxygen fugacities (Lepage, 2003; Lattard et al., 2005). We used the ILMAT program (Lepage, 2003) for 25 coexisting magnetite-ilmenite pairs from both Korab Kansi and Abu Ghalaga ores to calculate re-equilibration solidus temperatures ranging from 420 to 527 °C and 674–740 °C, respectively. The Abu Ghalaga ores, mainly hemo-ilmenite, have higher equilibration temperatures than those of the Korab Kansi, which are mainly magnetite. In addition,

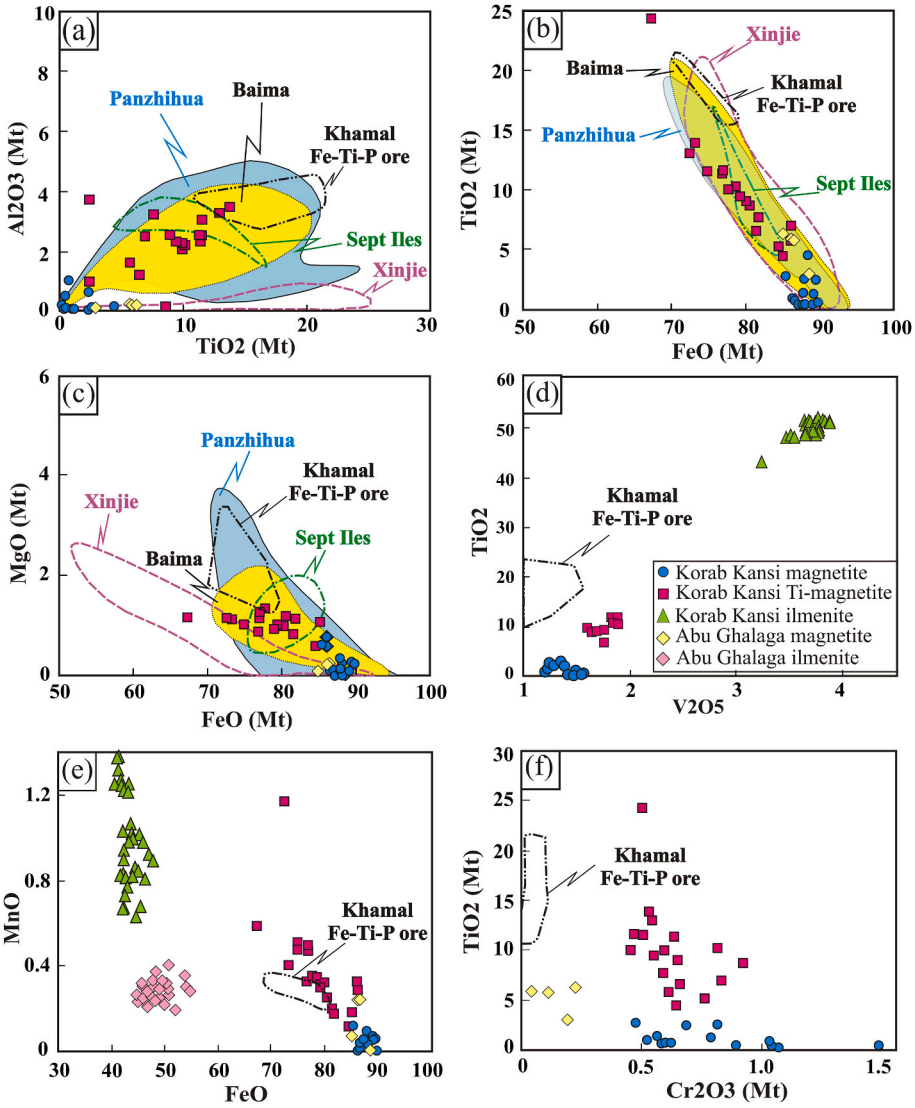


**Fig. 7.** Comparison between the SED Fe–Ti–V oxide minerals and worldwide magnetites from other layered intrusions. **a**) $TiO_2$ vs. $Al_2O_3$. **b**) FeO vs. $TiO_2$ (**c**) FeO vs. MgO. **d**). $V_2O_5$ vs. $TiO_2$ variation diagram. **e**) FeO vs. MnO. **f**) $Cr_2O_3$ vs. $TiO_2$. Magnetite data of Panzhihua (Pang et al., 2008; Song et al., 2013), Baima (Shellnutt and Pang, 2012; Zhang et al., 2012), Xinjie (Wang et al., 2008), Khamal Fe–Ti–P ores in the gabbro-anorthosite complex in the ANS (Eldougdoug et al., 2020) and Sept Iles (Namur et al., 2010) layered intrusions were used for comparison.

calculated oxygen fugacities ($f_{O2}$) are around ΔFMQ–1.24 to −3.28 for Korab Kansi ores and from ΔFMQ +0.21 to −0.3 for Abu Ghalaga ores based on results from ILMAT (Lepage, 2003) and reported as log units relative to the fayalite–magnetite–quartz buffer (FMQ). These oxygen fugacity results may represent solidus equilibrium conditions, but do not directly indicate magmatic conditions.

The higher $f_{O2}$ for Abu Ghalaga ores than for Korab Kansi ones is consistent with the high abundance of hematite in the former (Fig. 4f–h) and absence in the latter (Fig. 3e–h). Thus, the different redox conditions of these two intrusions was responsible for high magnetite content of titanomagnetite–magnetite series (Fig. 3e–h) in Korab Kansi ores and hematite content of ilmenite–hematite series in Abu Ghalaga ores (Fig. 4f–h; Supplementary 3) (e.g. Buddington and Lindsley, 1964; Lattard et al., 2005).

The Ti + V and Al + Mn contents of magnetite can be used as indicators of formation temperature (Dupuis and Beaudoin, 2011; Nadoll et al., 2014). The Korab Kansi magnetite data mostly plot around 300–500 °C based on Ti + V versus Al + Mn diagram (Supplementary 7b), suggesting that magnetite re-equilibrated at solidus conditions of *T*, ~500 °C or more. Another exsolution texture seen in Korab Kansi Fe–Ti–V oxide deposits is intergrowth of aluminous spinel and titanomagnetite (Fig. 3e), which occurs below ~600 °C (Vincent et al., 1957; Turnock and Eugster, 1962).

The Al content of primary amphiboles in Fe–Ti–V oxide deposits is sensitive to pressure (Schmidt, 1992). The application of this barometer yields average pressures of 8.3 kbar (27 km deep) for Korab Kansi ores and 5.1 kbar (17 km deep) for Abu Ghalaga ores (Supplementary 2). These results are consistent with occurrence of Fe–Ti–V oxides in the most primitive rocks (e.g. dunites and troctolites; Fig. 3) in the lower part of the Korab Kansi intrusion relative to Abu Ghalaga norites and anorthosites. The plagioclase + ilmenite ± magnetite assemblage and textures of Abu Ghalaga ores (Fig. 4) resembles that of Tellnes and Lac Tio deposits, which crystallized from ferrobasaltic melts at lower pressure (5–8 kbar) (Charlier et al., 2006, 2010; Supplementary 8).

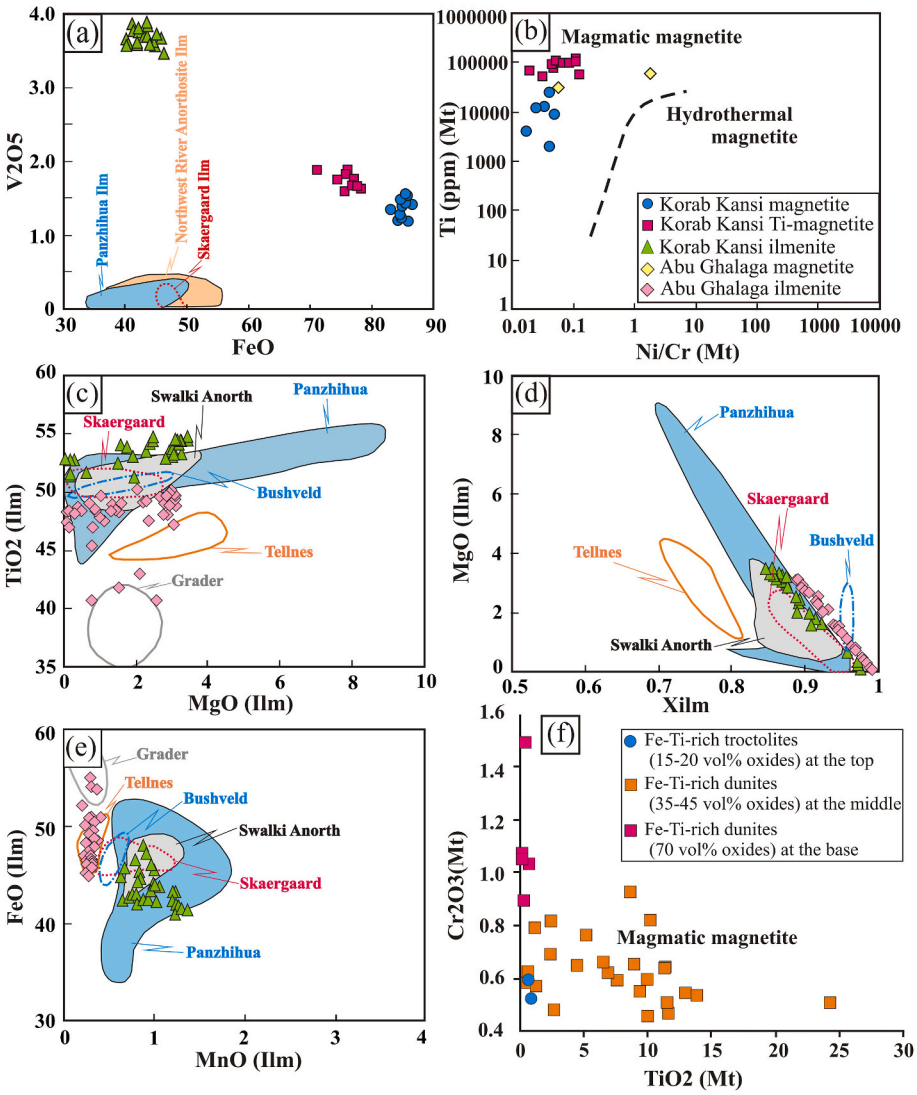


**Fig. 8.** Comparison between SED Fe–Ti–V oxide minerals and ilmenites from other layered intrusions. **a**) FeO vs.$V_2O_5$ for the SED magnetite and ilmenite. **b**) Ni/Cr vs. Ti binary diagram for the SED magnetite (Dare et al., 2014). **c**) MgO vs. $TiO_2$. **d**) $X_{ilm}$ vs. MgO. **e**) MnO vs. FeO. **f**) $TiO_2$ vs $Cr_2O_3$ diagram based on occurrence of magnetite in the base, middle and top of massive to disseminated ore layers in the base of the Korab Kansi layered intrusion. Ilmenite data of Panzhihua (Guan, 2014), Keating hill (Hinchey, 2015), Northwest River Anorthosite (Valvasori et al., 2020), Skaergaard (Jang and Naslund, 2003), Grader (Charlier et al., 2008), Suwalki (Charlier et al., 2009) and Tellnes (Charlier et al., 2006, 2007, 2015) layered intrusions were used for comparison.

### 6.4. *Genesis of Fe–Ti–V ore deposits in SED layered intrusions*

#### 6.4.1. *Magma type and tectonic setting*

The occurrence of Fe–Ti oxides between cumulus olivine (Figs. 2f and 3a) in the most primitive rocks (e.g. dunites and troctolites) indicates enrichment of their parent melts in Mg, Fe and Ti from the mantle source (host of Fe and Mg), similar to the Panzhihua intrusion (Bai et al., 2014; Pang et al., 2008). The olivine forsterite range ($Fo_{69-86}$; Khedr et al., 2020) and Cpx REE (Fig. 10c) of the Korab Kansi rocks resemble olivine $Fo_{79-88.9}$ and Cpx REE of Lalibela ferropicrites derived from a mantle source (Desta et al., 2014). The Korab Kansi olivine is similar in composition to olivines in MORB ferropicrites and Parana'–Etendeka ferropicrites (Tuff et al., 2005)(Fig. 5a), while the Cpx Al, Ti and Mg# plot mainly in the overlapping Cpx field of ferropicrites and ferrobasalts (Fig. 5c and d). The Korab Kansi gabbroic intrusion and its Fe–Ti–V ore deposits crystallized from ferropicritic or ferrobasaltic magmas, similar to the Panzhihua gabbroic layered intrusion hosted Fe–Ti–V oxide deposits that formed from highly evolved Fe–Ti–V-rich ferrobasaltic or ferropicritic magmas (Zhou et al., 2005) (Supplementary 8).

On the other hand, Abu Ghalaga Cpx Al, Ti and Mg# resemble those of tholeiitic ferrobasalts (Fig. 5c and d) (Leterrier et al., 1982; Lustrino, 2006; Namur et al., 2012). The Abu Ghalaga Opx is similar in Ti, Ca, Al and Mg# to ferrobasalt Opx (Fig. 6a and b) (Morisset, 2008; Charlier et al., 2010; Namur et al., 2012). In addition, REE-normalized U-shaped patterns of Abu Ghalaga ilmenite ores (Fig. 9a) are similar to those of Saint-Urbians and Big Island ilmenite hosted by anorthosites, thought to have originated from ferrobasaltic melts (Morisset, 2008; Morisset et al., 2010). CI-normalized REE patterns of Cpx in Abu Ghalaga ilmenitites are convex upward, similar to Cpx REE patterns of Sept Iles layered Fe–Ti–V oxide-bearing troctolites that crystallized from Fe-rich tholeiitic basaltic parent magmas (Namur et al., 2011). REE patterns of Opx and Cpx in Abu Ghalaga are also similar to those of the Motaghairat (Fig. 9e) layered intrusion, which is thought to have crystallized through fractional crystallization from high-Mg tholeiitic melts (e.g., ferrobasaltic melts) derived from a metasomatized mantle source in the rift setting

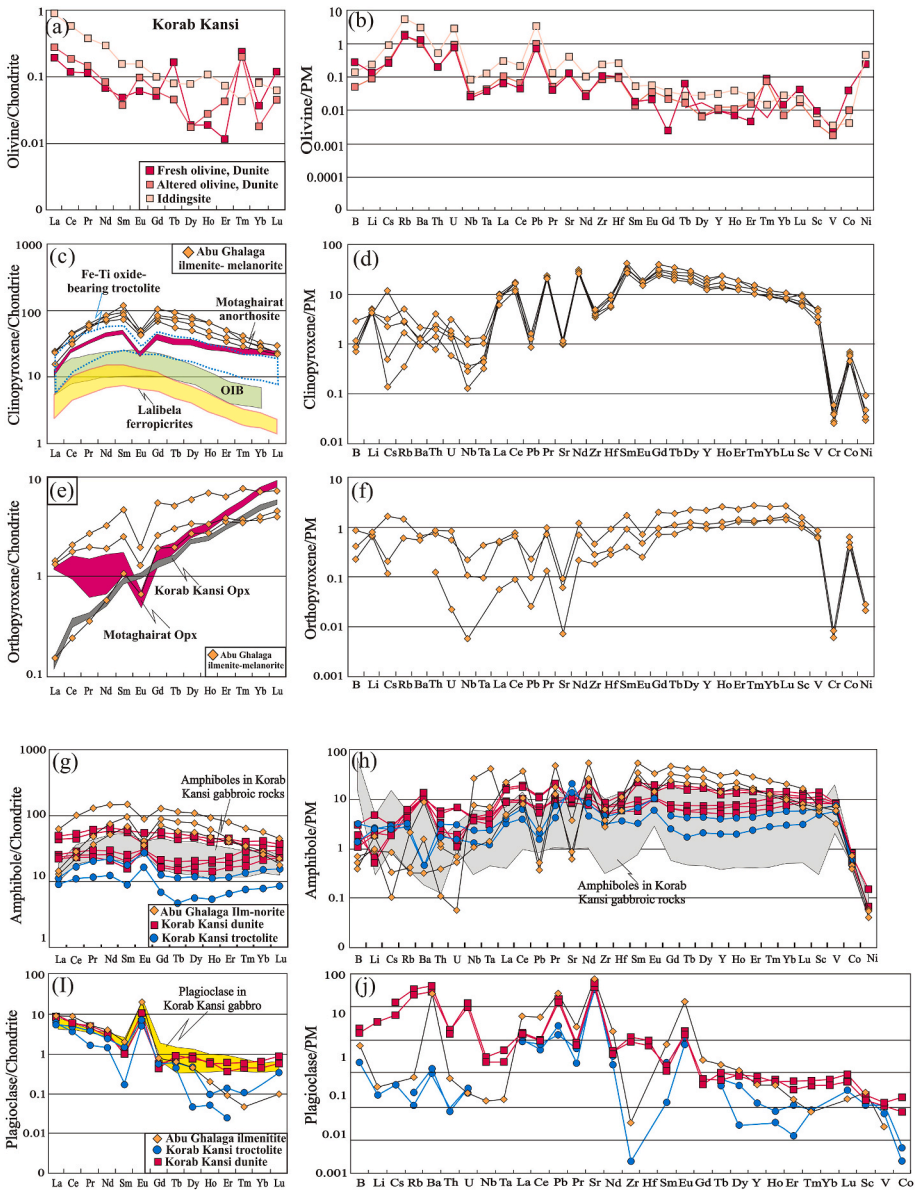


**Fig. 9.** Trace and REE patterns of silicate minerals in Korab Kansi and Abu Ghalaga Fe–Ti–V ore deposits. Chondrite (CI)-normalized REE patterns **(a, c, e, g, i)** and primitive mantle (PM)-normalized trace-element patterns **(b, d, f, h, j)** for olivine, Cpx, Opx, amphiboles and plagioclase of Abu Ghalaga and Korab Kansi Fe–Ti oxide ores. The purple fields in panels **(c, e)** represent Cpx and Opx of the Motaghirat anorthosites (Abdel Halim et al., 2016), while the dark grey field represents Opx of Korab Kansi ultramafic rocks (Khedr et al., 2020). The pale grey fields in panels **(g, h)** represent amphiboles of the host Korab Kansi gabbroic rocks and plagioclase in the Korab Kansi after Khedr et al. (2020). The Cpxs in ocean-island basalts (OIB; Nimis and Vannucci, 1995), Lalibela ferropicrites (Desta et al., 2014) and Fe–Ti oxide-bearing troctolites from the Sept Iles layered intrusion (Quebec, Canada; Namur et al., 2011) are used for comparison. Chondrite (CI) and primitive mantle (PM) values are from McDonough and Sun (1995).

(Abdel Halim et al., 2016). The equilibrated melt composition of Abu Ghalaga Cpx (Fig. 11a) was calculated using Cpx/melt partition coefficients (Hart and Dunn, 1993; Johnson, 1998). Its chondrite-normalized REEs (McDonough and Sun, 1995) show inclined patterns with decreasing REE contents from LREE to HREE, like those of tholeiitic basalts derived from mantle melting (Clift and Fitton, 1998) and ocean-island basaltic melts (Sun and McDonough, 1989) (Fig. 11a). This chemical features suggest tholeiitic ferrobasaltic parent melts of Abu Ghalaga Fe–Ti ores, possibly generated in a subduction-related rift setting (Fig. 12).

Magnetite trace-element compositions can be used to distinguish different iron deposits such as iron oxide-copper-gold (IOCG), porphyry Cu, Kiruna, BIF, skarn, and Fe–Ti–V deposits (Dupuis and Beaudoin, 2011; Dare et al., 2014; Knipping et al., 2015). The Korab Kansi magnetite belongs to magmatic Fe–Ti–V deposits based on its Cr, V, Ti, Ni, Al, Mn and Cr compositions (Supplementary 7a-c). Its trace-element patterns (Fig. 11b) and textures (Fig. 3) resemble Panzhihua and Baima magmatic magnetites crystallized from Fe–Ti–V-rich ferropicritic or ferrobasaltic magmas (Zhou et al., 2005; Bai et al., 2014; Luan et al., 2014; Liu et al., 2015; Wang et al., 2014). The ilmenite and titanohematite trace-element patterns show strong positive HFSE anomalies (Ti, Nb, Ta, Zr and Hf), V and Sc, while Abu Ghalaga ilmenite is highly enriched in Nb, Ta, and Hf (Fig. 10). This enrichment of incompatible elements (HFSE) in SED Fe–Ti oxides (Fig. 10) is attributed to their Fe–Ti rich parent melts that were rich in these elements and derived from a mantle source, like plume-derived ferropicrites (Goldstein and Francis, 2008; Bai et al., 2014). This suggests that ferropicritic/ferrobasaltic parent melts of SED Fe–Ti oxides (Fig. 10; Supplementarys 3–5) were

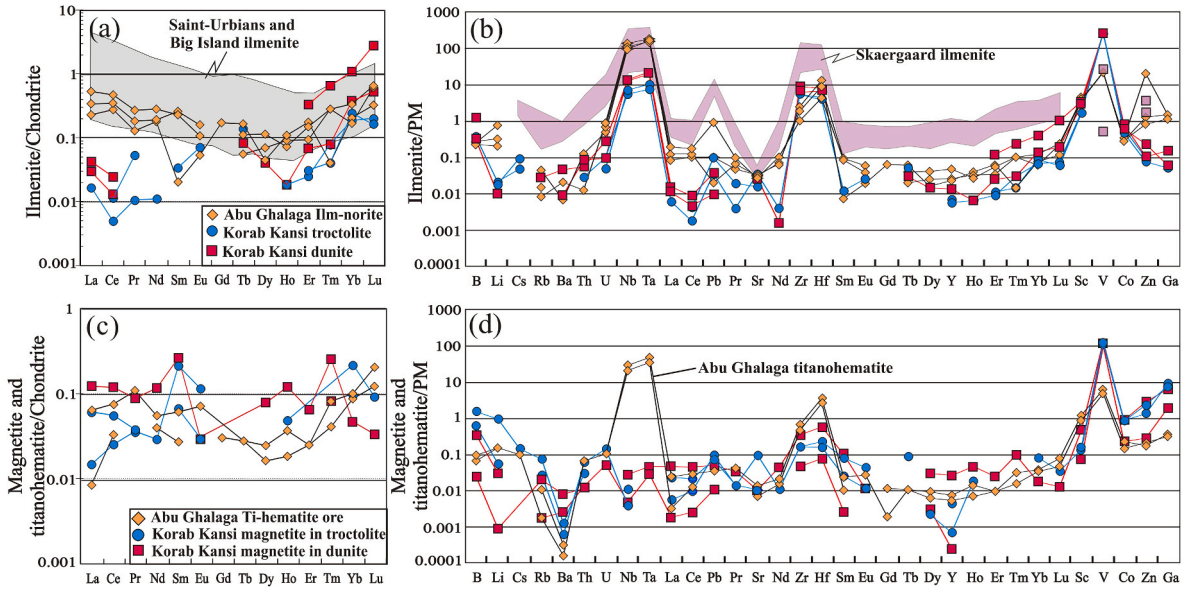


**Fig. 10.** Trace and REE patterns of Korab Kansi and Abu Ghalaga Fe–Ti–V oxide minerals. Chondrite (CI)-normalized REE patterns **(a, c)** and primitive mantle (PM)-normalized trace-element patterns **(b, d)** for ilmenite, magnetite and hematite from Abu Ghalaga and Korab Kansi Fe–Ti oxide ores. The purple field in panel (**b**) represents Skaegaard ilmenite (data after Jang and Naslund, 2003). Saint-Urbians and Big Island ilmenite field (Morisset, 2008; Morisset et al., 2010) is used for comparison. Normalized chondrite (CI) and primitive mantle (PM) values are from McDonough and Sun (1995).

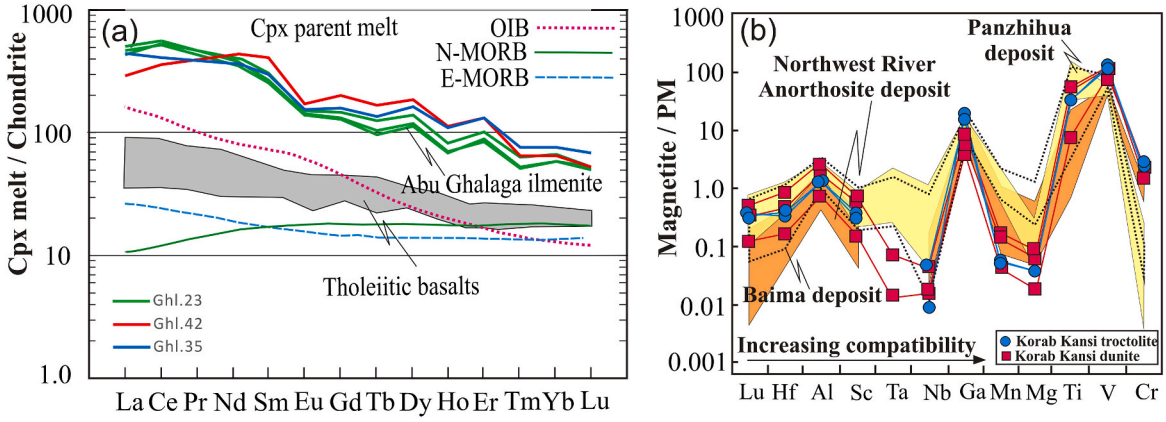


**Fig. 11.** **a**) CI-normalized REE patterns for calculated melts in equilibrium with Cpx from Abu Ghalaga Fe–Ti–V oxide ores. Cpx/melt partition coefficients are from Hart and Dunn (1993) and Stosch (1982). Normal mid-ocean ridge basalt (N-MORB), Ocean island basalt (OIB) and enriched mid-ocean ridge basalt (E-MORB) compositions are from Sun and McDonough (1989). REE patterns of tholeiitic basalts crystallized from mantle-derived melts (Clift and Fitton, 1998) are used for comparison. Normalized C1 and PM values are from McDonough and Sun (1995). **b**) PM-normalized lithophile elements for the Korab Kansi magnetite compared with magnetite from Panzhihua, Baima and Northwest River Anorthosite intrusions. Data of Panzhihua and Baima are from Liu et al. (2015), while data for Northwest River Anorthosite are from Valvasori et al. (2020).

derived mainly from the upper mantle during interaction between metasomatized lithosphere and upwelling asthenosphere or a mantle plume (Fig. 12). This is consistent with global ferropicritic or ferrobasaltic melts, which are enriched in Fe and HFSE and are related to anomalously hot mantle such as upwelling asthenosphere or mantle plumes (Hanski and Smolkin, 1995; Goldstein and Francis, 2008) (Fig. 12). The parent melts of Fe–Ti oxides are enriched in Nb, Ta, Ti and V (Figs. 10 and 11), reflecting significant contributions from a mantle-plume source (Condie, 1997). They are also poor in Ni, Cr, Co and Mn with subordinate S and Cu (Figs. 3, 4 and 10; Tables 2 and 3; Supplementarys 3–5). Active rifting in convergent margin settings sometimes results from slab breakoff associated with upwelling asthenosphere or a mantle plume, which is forcefully injected into the base of the metasomatized lithosphere in the studied areas (Fig. 12). During injection, diapirs undergo adiabatic decompression leading to partial melting and generation of parent melts of SED layered intrusions (Fig. 12).

Picrites are found in different tectonic environments: midocean ridges, continental rifts and arcs like the Lesser Antilles Island Arc (e.g., Woodland et al., 2002), Solomon Islands (e.g., Ramsay et al., 1984) and Vanuatu Arc (e.g., Eggins, 1993). Some features of Korab Kansi and Abu Ghalaga ores are best explained by formation or modification above a

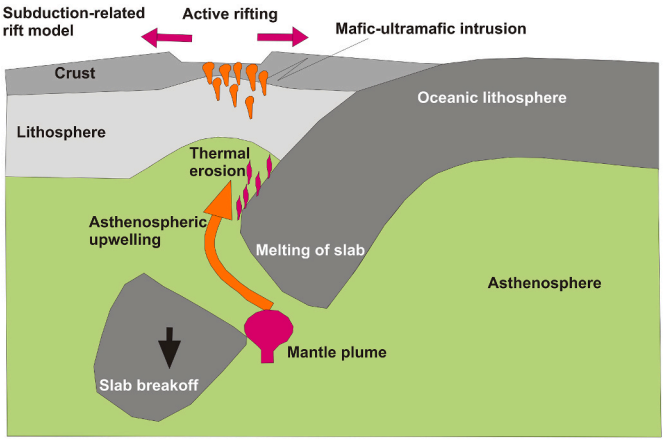


**Fig. 12.** Sketch of subduction-related rift model (modified after Merle, 2011) for the origin of mafic-ultramafic intrusions in the SED of Egypt. Active rifting is due to slab breakoff and upwelling of asthenosphere or mantle plumes.

subduction zone. The Abu Ghalaga and Korab Kansi layered intrusions are associated with island-arc assemblages in the field (Khedr et al., 2020). Nisbet and Pearce (1977) calculated two equations for clinopyroxene compositions to indicate different tectonic settings. The Abu Ghalaga Cpx compositions plot in the fields of volcanic arc based on $F_1$ vs. $F_2$ digaram (Fig. 5e) after Nisbet and Pearce (1977) or island arc basalt (Beccaluva et al., 1989) (Fig. 5f), suggesting the subduction-related rift setting (Fig. 12). PM-normalized Cpx patterns show depletion in HFSE (e.g., Nb, Ta, Zr and Hf; Fig. 9d), suggesting a convergent margin setting (or SSZ: suprasubduction zone) of the investigated SED intrusions. This is consistent with U-shaped REE patterns of amphiboles in Korab Kansi Fe–Ti–V oxide ores (Fig. 9g), which are like those of SSZ amphiboles (Khedr et al., 2010). Amphiboles are rich in Rb, Ba, Sr, U, La, Ce and Pr (Fig. 9h) and olivines show positive anomalies for Pb, Ba, Sr, Rb and U, indicating these crystallized from hydrous parental melts dominated by slab-derived fluids in a convergent margin setting (Fig. 9b).

Finally, highly oxidizing conditions due to high aqueous $H_2O$ contents are consistent with generation of Korab Kansi and Abu Ghalaga intrusions in a rift-related convergent margin setting (Fig. 12). The composition of ferrobasaltic/ferropicritic parental magmas of the investigated oxide deposits was the main factor causing deposition of Fe–Ti rich layers, similar to Fe–Ti oxide ores in Panzhihua, Baima and Hongge intrusions (Zhou et al., 2005; Zhang et al., 2009; Luan et al., 2014; Liu et al., 2015) (Supplementary 8). Composition of parental magmas, high oxygen fugacity ($f_{O2}$) conditions and high $H_2O$ contents of the magmas are proposed to have been controlling factors for generating economic Fe–Ti–V oxides ore layers in SED mafic-ultramafic intrusions. These factors also cause compositional (Figs. 3 and 4; Supplementary 3) and trace-element variations (Fig. 10) of SED Fe–Ti–V oxide deposits.

### 6.4.2. *Evidence of fractional crystallization and immiscible separation of melts*

Several theories have been proposed to explain the formation of global economic Fe–Ti ore deposits and host silicate layers: 1) fractional crystallization either by crystal settling (Martin, 1990; Charlier et al., 2006, 2015) and/or in situ crystallization (Campbell, 1978; McBirney and Noyes, 1979; Latypov et al. 2016, 2020; Kruger and Latypov, 2020), 2) immiscible separation of oxide melts from magma and their accumulation with floating of plagioclase crystals (Force, 1991; Von Gruenewaldt, 1993), and 3) magma mixing and polybaric crystallization (Morisset et al., 2010; Charlier et al., 2015). Magma mixing can produce hybrid magmas and crystallize a pure ilmenite cumulate (Charlier et al., 2015), but not the rocks we describe. Therefore, fractional crystallization and immiscible separation better explain the origin of Fe–Ti oxides and host silicate layers in SED intrusions (Fig. 13).

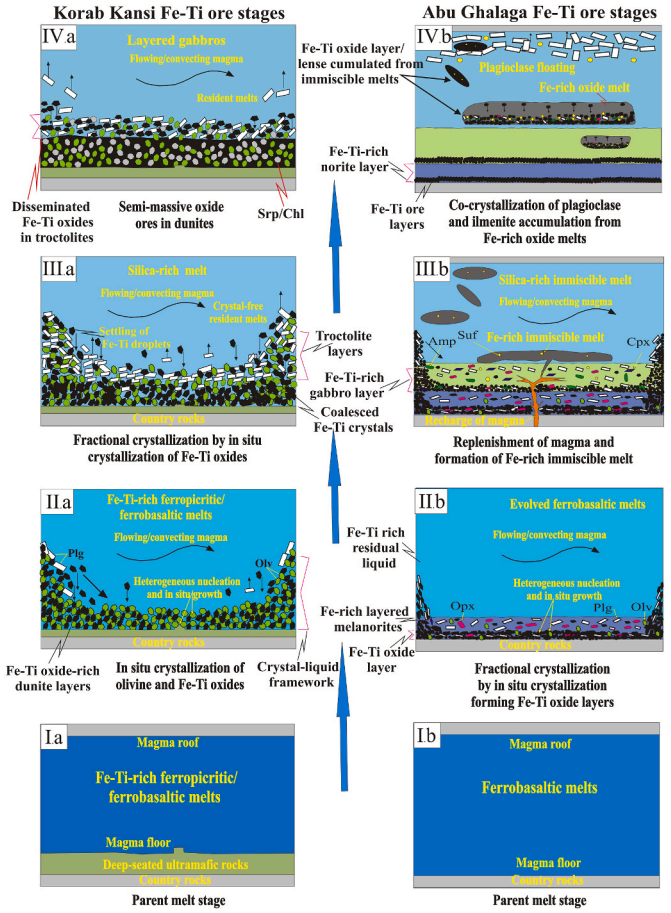


**Fig. 13.** Schematic illustration showing how Abu Ghalaga (right) and Korab Kansi (left) Fe–Ti–V oxide ores formed. The Korab Kansi Fe–Ti oxide ores crystallized from ferropicritic melts at an earlier stage of fractionation than Abu Ghalaga ores. Fractional crystallization by in situ crystallization accompanied with crystal settling and accumulation of Fe–Ti oxide crystals was dominated in the Korab Kansi, whereas fractional crystallization followed by segregation of an immiscible Fe-rich melt and co-crystallization of Fe–Ti oxides with flotation of plagioclase was responsible for the origin of Abu Ghalaga ore deposits. Abbreviation of Opx: orthopyroxene; Cpx: clinopyroxene; Olv: olivine; Plg: plagioclase; Suf: sulfides; Amp: amphiboles.

The Korab Kansi Fe–Ti–V ore deposits are concordant layers in host dunites and troctolites near the base of a layered intrusion (Fig. 2), suggesting their origin by fractional crystallization. Their fractional crystallization origin is confirmed from: 1) dominant layered structure of the oxide ores (Fig. 2a–d) with cumulus olivine (Figs. 3), 2) decreasing plagioclase A content and amphibole Mg# (0.97, 0.79, 0.77, 0.69 and 0.64 on average) for peridotites, troctolites, pyroxene gabbros, gabbronorites and pyroxene-hornblende gabbros from the base to the top of the Korab Kansi intrusion (Khedr et al., 2020), 3) some plagioclase grains are zoned (Fig. 3d), suggesting separation from an evolving liquid (e.g., Brown, 1993), 4) systematic decreasing of Cr in magnetite from the base of the intrusion to the most evolved rocks (Figs. 7f and 8f; Supplementary 3) (e.g., Liu et al., 2015), and 5) lower olivine Fo content (69.8 mol%) of Korab Kansi Fe–Ti–V oxide-rich troctolites than olivine Fo (72.9 mol% on average) of Fe–Ti–V oxide-rich dunites (Supplementary 2). The lower forsterite content ($Fo_{68.8\text{-}74.2}$) of olivine in Korab Kansi Fe–Ti–V ores (Fig. 5a; Table 1, Supplementary 2) than surrounding peridotite olivines ($Fo_{85.5\text{-}86}$) and fine-grained olivine gabbros ($Fo_{77.7\text{-}78.7}$) as a chilled margin (Khedr et al., 2020) suggests that these ores crystallized from more fractionated ferropicritic or ferrobasaltic melts (Fig. 13). The origin of Korab Kansi Fe–Ti–V oxide layers by fractional crystallization may be explained either by in situ

crystallization (e.g., Latypov et al., 2016) and/or crystal settling (e.g. Martin, 1990).

Based on field observations and petrography, Fe-rich dunites at the base of the Korab Kansi intrusion have higher concentration of Fe–Ti oxides (60–70 oxide vol%; Fig. 3a) than Fe-bearing dunites (35–45 vol %) in their upper part, where Fe–Ti oxide concentrations gradually decrease upward to Fe-bearing troctolite (Fig. 3b and c; 15–20 vol%) layers and pyroxene gabbros (<15 oxide vol%; Fig. 3d). This may be related to settling of crystals to the magma chamber floor (Fig. 13), forming high Fe–Ti oxide concentrations at the base (Figs. 2 and 3a). Moreover, average olivine size decreases slightly from Fe-rich dunites (1.5 mm across) to Fe-bearing dunites (1.2 mm) and Fe-bearing troctolite (<1 mm across) (Fig. 3a–d), showing slightly graded bedding. These two observations suggest fractional crystallization via crystal settling.

The systematic decrease of $V_2O_5$ and $Cr_2O_3$ in magnetite from the base of Fe–Ti semi-massive ores ($V_2O_5$ = 1.8 wt%; $Cr_2O_3$ = 1.5 wt%) to the top of disseminated ores ($V_2O_5$ = 1.2 wt%; $Cr_2O_3$ = 0.48 wt%) (Fig. 8f; Table 2; Supplementary 3) is evidence for in situ crystallization (e.g., Kruger and Latypov, 2020). The sharp upward depletion in Cr of SED magnetite is similar to a steep upward depletion in Cr content of magnetite in the Bushveld Complex magnetite layer, where magnetite started to nucleate and grow, providing evidence for in situ crystallization (Kruger and Latypov, 2020). Therefore, fractionation by in situ crystallization may have been more important than crystal settling for accumulating Fe–Ti oxide ores at the base of the Korab Kansi layered intrusion.

The Fe–Ti oxide crystals grew in situ between cumulus olivine (Fig. 3a, f) beneath the magma chamber floor (Fig. 13. IIa-IVa), accompanying gravity settling of some crystals (e.g., Martin, 1990) that segregated from Fe–Ti-rich parent melts. These crystals descended into the unconsolidated crystal pile, pushing out lower density interstitial melts and filling some interstices between cumulus silicates (Fig. 3a, f, 13a). Fractional crystallization by in situ crystallization and crystal settling may form the cumulate stratigraphy of the Korab Kansi intrusion and associated ore deposits (Fig. 13a).

On the other hand, fractional crystallization by in situ crystallization of ferrobasaltic melts associated with liquid immiscibility could have produced layers and lenses of Fe–Ti oxides, and layers of melanonorites, gabbros and anorthosites in the Abu Ghalaga intrusion and residual liquids (Fig. 13b). These residual liquids may have separated into conjugate Si-rich and Fe–Ti- rich melts (e.g., Force, 1991; Von Gruenewaldt, 1993). The latter melts could have produced Abu Ghalaga Fe–Ti oxide lenses associated with plagioclase flotation, forming economic hemo-ilmenite ores (Fig. 4f–h) in sharp contact with anorthosites (Fig. 4a). In this scenario, massive ore layers near the base of the intrusion could have been produced by in situ crystallization beneath the magma floor (Fig. 13b). Other scattered lenses and pods of net textures in the middle (e.g., norites) and upper sectors (e.g., anorthosites) of the intrusion precipitated as cumulates from immiscible oxide melts (Fig. 13b). Evidence for in situ crystallization of Abu Ghalaga massive ores at the base of the intrusion includes: 1) Few Abu Ghalaga ilmenite ore layers include autoliths of host norites and anorthositic gabbros (Basta and Takla, 1968), like anorthosite autoliths within the in situ crystallized magnetite deposits in the Bushveld Complex (Kruger and Latypov, 2020). 2) Interstitial hemo-ilmenites between idiomorphic primocrysts of Opx and edenite in ilmenite-rich melanorites (Fig. 4b) and dendritic oikocrysts of edenite and Cpx that enclose chadacrysts of Fe–Ti oxides (Fig. 4d) are evidence for in situ crystallization in the liquid-crystal framework (e.g., Kruger and Latypov, 2020; Latypov et al., 2020). 3) Plagioclase crystals were less dense than residual Fe–Ti-rich liquids (Fig. 13), however, they occur on the floor of the Abu Ghalaga intrusion (Fig. 4b), reflecting in situ crystallization from some trapped melts (e.g., McBirney and Noyes, 1979).

Some ilmenite lenses in the middle and upper parts of the Abu Ghalaga intrusion likely originated from Fe-rich melts that separated from a silicate-rich melt via liquid immiscibility of ferrobasaltic parent melts (e.g., Morisset et al., 2010; Charlier et al., 2010, 2015) (Fig. 13 b). Other lines of evidence supporting liquid immiscibility include: 1) Ilmenite lenses and inclined sheet-like pods in the middle and near the top of the Abu Ghalaga intrusion (Fig. 1d, Supplementary 1b) suggest liquid immiscibility and segregation of conjugate Si-rich (forming anorthosite) and Fe-rich melts, from which Fe–Ti oxide accumulated (Fig. 4a, e, 13b) (Philpotts, 1967; Charlier et al., 2015). 2) The reactive symplectite growth (Fig. 4c) is due to the movement of two immiscible melts such as Si-rich and Fe–Ti-rich melts (Dong et al., 2013), similar to the formation of symplectite during the last solidification stage of the Skaergaard, Sept Iles and Xinjie (SW China) layered intrusions (Holness et al., 2011; Dong et al., 2013; Keevil et al., 2020) as well as symplectite fabrics in Ediacaran (post-collisional) gabbros from the Ablah-Shuwas belt in the western Arabian Shield of Saudia Arabia (Surour et al., 2017). This symplectite (Fig. 4c) may have formed due to reaction between plagioclase primocrysts in Abu Ghalaga gabbros and immiscible Fe–Ti melts (e.g., Scoon et al., 2017). The occurrence of this symplectite (Fig. 4c) consists with symplectite textures that are a common feature of layered gabbroic intrusions in the Arabian-Nubian Shield (Surour et al., 2017; Habtoor et al., 2022). 3) Abundance of sulfide droplets or coarse grains (Fig. 4e–h) associated with apatite (Fig. 4g) in Fe–Ti oxides reflects Fe–Ti–P and S liquid immiscibility (e.g., Ripley et al., 1998) and higher volatile contents (e.g. S, P, F and Cl) as fluxing agents, which facilitated the development of late stage immiscible liquids (Zhou et al., 2005; Zhang et al., 2009; Chen et al., 2013; Eldougdoug et al., 2020). 4) Abundance of amphiboles in Fe–Ti ores (Fig. 4d) suggests the hydrous nature of parental melts from which Fe–Ti oxide melts separated by immiscibility (Zhou et al., 2005). These observations support a role for immiscible liquid separation and crystal accumulation from Fe-rich melts, in addition to the in-situ growth origin of Fe–Ti oxides of massive ores at the base of the Abu Ghalaga intrusion (Fig. 13b).

Finally, abundant plagioclase (15–50 modal vol%) and sulfide (3–5 vol%) in Abu Ghalaga (Fig. 4) ores with high REE contents of Cpx (ΣREEs = 125.4–150.9 ppm), amphibole (ΣREEs = 101–264.3 ppm), plagioclase (ΣREEs = 15.61 ppm) and ilmenite (ΣREEs = 0.55–0.81 ppm; Nb = 62.4–72.6 ppm; Ta = 5.6–5.7 ppm) (Fig. 9c–g, 10a; Table 3, Supplementary 5) relative to Korab Kansi ores (Fig. 3) suggest the more fractionated parent melts of the former. The alternation of the Fe–Ti–V oxide multiple layers with Fe–Ti oxide-bearing gabbros (Fig. 2a) within a single zone of the intrusion suggests multiple recharge of Fe–Ti-rich magmas during formation of SED layered intrusions, similar to those described in the Baima and Hongge intrusions (Bai et al., 2012; Zhang et al., 2012).

### 6.5. Enrichment of vanadium in Korab Kansi Fe–Ti ore deposits

The partition coefficient of V in magnetite decreases with increasing oxygen fugacity ($f_{O2}$) in contrast to ilmenite because $V^{+4}$ substitutes for $Ti^{+4}$ (Toplis and Corgne, 2002). The $f_{O2}$ of Korab Kansi mafic-ultramafic magmas was high (FMQ +4.1 to FMQ +4.3) (Khedr et al., 2020) and this can explain why vanadium is strongly partitioned into Korab Kansi ilmenite (3.1–3.8 wt% $V_2O_5$) relative to magnetite ($V_2O_5$, 1.2–2.0 wt%; Fig. 7d) and strongly correlates with Ti in both minerals (Fig. 7d, Supplementary 3). The experiments of Schuiling and Feenstra (1980) also show that vanadium preferentially partitions into ilmenite at oxygen fugacities higher than normally found in silicate melts, like the highly oxidizing condition of Korab Kansi ore formation.

A common feature of Korab Kansi magnetite is vanadium enrichment ($V_2O_5$, 1.2–2.0 wt%; Supplementary 3), similar to V-rich magnetite found in the Fe–Ti–V oxide deposits of Mustavaara ($V_2O_5$, 1.27–1.76 wt %; Taipale et al., 2013), Skaergaard ($V_2O_5$<1.74 wt%; Jang et al., 2001), Bushveld Complex (2.0–2.2 wt% $V_2O_5$; Scoon et al., 2017) and Sinarsuk ($V_2O_5$, 1.93–2.68 wt%; Grammatikopoulos et al., 2002) layered intrusions. $V^{+3}$ can replace $Fe^{+3}$ in magnetite, where it negatively correlates with Fe (Fig. 8a). The Korab Kansi titanomagnetite (V:

7840–10250 ppm) and ilmenite (V: 20600-21850 ppm) are rich in V relative to that (V: 1234–3127 ppm) in magnetite-ilmenite in the Khamal complex in the Arabian Shield (Eldougdoug et al., 2020) (Table 3, Supplementary 5), reflecting Korab Kansi V-rich parent melts. Therefore, the much higher V contents in Korab Kansi ores may be due to the V-rich nature of ferropicritic or ferrobasaltic parental melts, high oxygen fugacity ($f_{O2}$) and high crystallization temperature ($T$, ~1180 °C) of the intrusion (e.g., Mallmann and O'Neill, 2009; Khedr et al., 2020). In the Korab Kansi, high $f_{O2}$ crystallization conditions of the original oxide crystals led to increased ilmenite exsolution in magnetite (Fig. 3g and h), which enhanced partitioning of vanadium in ilmenite (Klemm et al., 1985; Taipale et al., 2013). This high $f_{O2}$ of Korab Kansi Fe–Ti oxides also causes saturation of titanomagnetite prior to ilmenite, and may reflect significant addition of $H_2O$ derived from a subducting slab into the mantle source region. Fe–Ti–V-rich regions in the Neoproterozoic mantle source may have been responsible for higher V contents in Korab Kansi ores, and are possibly due to interaction of lithosphere with upwelling asthenosphere or mantle plumes, forming mantle heterogeneity beneath Arabian-Nubian Shield (Khedr et al., 2020).

The Abu Ghalaga ores were generated under very oxidizing conditions, as shown by abundant hematite lamellae in ilmenite (Fig. 4f–h). Their high oxygen fugacity ($f_{O2}$, ~ ΔFMQ +0.21 to −0.3) increases the magmatic $Fe_2O_3$/FeO ratio, forming abundant hemo-ilmenite (Fig. 4f–h). The highly oxidizing nature of Abu Ghalaga parental magmas was responsible for the relatively low vanadium content (Table 3) of hematite and hemo-ilmenite (e.g., Charlier et al., 2009), beside the depletion of V in the parental melt. V and Ti are immobile in slab-derived fluids and unlikely to be added to Korab Kansi and Abu Ghalaga mantle sources (Green and Adam, 2003; Spandler et al., 2007; Khedr et al., 2020). Therefore, the V in magnetite and ilmenite was controlled by vanadium concentration in parental melts and oxidizing conditions.

## 7. Conclusions

1. The Korab Kansi ores (titanomagnetite with subordinate ilmenite) occur mainly as concordant layers in host dunites and troctolites, whereas Abu Ghalaga deposits (hemo-ilmenite) are found as lenses and layers hosted in norites, gabbros and anorthosites.
2. The Korab Kansi ilmenite and titanomagnetite has higher vanadium concentrations compared with well-known worldwide Fe–Ti–V oxide deposits due to the parent magmas, being V-rich ferropicrites or ferrobasalts with high oxygen fugacity ($f_{O2}$). The V-rich nature of these magmas suggests that the Neoproterozoic mantle beneath the Arabian-Nubian Shield was very heterogeneous, with regions that were Fe–Ti–V-rich and had high $f_{O2}$. This Fe–Ti–V-rich mantle may be due to upwelling of a mantle plume or asthenosphere beneath the Arabian-Nubian Shield.
3. The Abu Ghalaga ilmenite is a high quality ore because of its low Cr and Mg content with significant hematite (8.7 mol% on average). Trace-element contents of Abu Ghalaga ores and sulfides are higher than those of Korab Kansi ores, reflecting more fractionated parental melts of the former.
4. The Korab Kansi ore deposits formed by fractional crystallization of Fe–Ti–V rich magmas and settling of dunitic cumulates accompanied by in situ crystallization of Fe–Ti oxides at the magma chamber floor. In contrast, as a result of more advanced fractionation, the Abu Ghalaga ferrobasaltic parent magmas immiscibly separated into a Si-rich melt, which formed anorthosite and a Fe–Ti rich oxide melt. The Abu Ghalaga massive Fe–Ti oxides at the base of the intrusion grew in situ from Fe–Ti-rich parent melts whereas most scattered lenses at the top precipitated from immiscible Fe–Ti-rich oxide melts that separated from the parental magma associated with floatation of plagioclase and sulfide.
5. Both Korab Kansi and Abu Ghalaga ore deposits formed from Fe–Ti rich magmas generated in a rift-related convergent margin setting through interaction between upwelling asthenospheric melts or mantle plumes and lithospheric mantle. The Korab Kansi ores formed early in the magmatic fractionation sequence and Abu Ghalaga ores formed late. The Abu Ghalaga gabbroic intrusion crystallized from ferrobasaltic magmas of tholeiitic affinity at lower temperature (~1082 °C) and pressure (~5 kbar) than the Korab Kansi intrusion (~1180 °C, 8.3 kbar).
6. The diversity in chemistry and mineralogy of SED Fe–Ti oxide deposits was strongly controlled by melt compositions and variations in $f_{O2}$ and $H_2O$ content of the parent melts. Magmatic concentration of Fe–Ti–V oxide ores in Korab Kansi and Abu Ghalaga requires Fe–Ti rich parental melts (ferropicritic/ferrobasaltic melts), and variations in the oxidation state of the magmas (high $f_{O2}$) due to addition of $H_2O$ to the magma source.

## Declaration of competing interest

The authors declare that they have no known competing financial interests or personal relationships that could have appeared to influence the work reported in this paper.

## Acknowledgments

The first and last authors gratefully acknowledge Mr. Ahmed Al Desouky for his help in the field work (during March and May 2018) in the South Eastern Desert and stay in Shalateen city. We thank Saif Abu Khashaba for preparing Landsat maps of Korab Kansi and Abu Ghalaga areas. This is UTD Geosciences contribution # 1670. We are grateful to Prof. Salah Al-Khirbash and the anonymous reviewers for their careful reading of our manuscript and their many insightful comments. We thank Prof. Prof. Read Mapeo (Editors-in-Chief) and Zakaria Hamimi (Associate Editor) for their editorial handling of this manuscript.

## Appendix A. Supplementary data

Supplementary data to this article can be found online at https://doi.org/10.1016/j.jafrearsci.2022.104620.

## References

Abdel-Gawad, G.M., 2002. Geological and Geochemical Characteristics of the Mafic-Ultramafic Rocks of Gabal Korab Kansi Area, South Eastern Desert, Egypt. Ph.D. Thesis. Zagazig University, p. 195.
Abdel Halim, A.H., Helmy, H.M., Abd El-Rahman, Y.M., Shibata, T., El Mahallawi, M.M., Yoshikawa, M., Arai, S., 2016. Petrology of the Motaghairat mafic-ultramafic complex, Eastern Desert, Egypt: a high-Mg post-collisional extension-related layered intrusion. J. Asian Earth Sci. 116, 164–180.
Amin, M.S., 1954. The ilmenite deposit of Abu Ghalqa, Egypt. Econ. Geol. 49, 77–87.
Bai, Z.J., Zhong, H., Naldrett, A.J., Zhu, W.G., Xu, G.W., 2012. Whole-rock and mineral composition constraints on the genesis of the giant Hongge Fe-Ti-V oxide deposit in the Emeishan Large Igneous Province, Southwest China. Econ. Geol. 107, 507–524.
Bai, Z.-J., Zhong, H., Li, C., Zhu, W.-G., He, D.-F., Qi, L., 2014. Contrasting parental magma compositions for the Hongge and Panzhihua magmatic Fe-Ti-V oxide deposits, emeishan large igneous province, SW China. Econ. Geol. 109, 1763–1785.
Basley, J.R., Buddington, A.F., 1958. Iron–titanium oxide minerals, rocks and aeromagnetic anomalies of the Adirondacks area, New York. Econ. Geol. 53, 777–805.
Basta, E.Z., Girgis, M.H., 1968. The mineralogy of titaniferous iron ores of Um Effin, South Eastern Desert, Egypt. The proceed of Egypt. Academy of Science 21, 127–144.
Basta, E.Z., Takla, M.A., 1968. Petrological studies on Abu Ghalaga ilmenite occurrence, Eastern Desert. J. Geol. 12, 43–72.
Basta, E.Z., Girgis, M.H., 1969. Petrological, mineralogical and geochemical studies on the magnetite-ilmenite-apatite ore (Nelsonite) from Kolmnab, South Eastern Desert, U.A.R. The proceed of Egypt. Academy of Science 22, 147–157.
Basta, E.Z., 1977. A comparative mineralogical study and classification of the titaniferous iron ores of Egypt. Bull. Sci. Cairo Univ. 46, 431–456.
Beccaluva, L., Maccoita, G., Piccardo, G.B., Zeda, O., 1989. Clinopyroxene composition of ophiolite basalts as petrogenetic indicator. Chem. Geol. 77, 165–182.
Bergeron, M., 1980. A mineralogical study of the hemo—ilmenite ore from Lac Tio, Quebec. Documentation Technique 5, 1–163.
Brey, G.P., Kohler, T., 1990. Geothermobarometry in four-phase lherzolites II. New thermobarometers, and practical assessment of existing thermobarometers. J. Petrol. 31, 1353–1378.

Brown, W.L., 1993. Fractional crystallization and zoning in igneous feldspars: ideal water-buffered liquid fractionation lines and feldspar zoning paths. Contrib. Mineral. Petrol. 113, 115–125.
Buddington, A.F., Lindsley, D.H., 1964. Iron-Titanium Oxide Minerals and Synthetic Equivalents.
Campbell, I.H., 1978. Some problems with the cumulus theory. Lithos 11, 311–323.
Charlier, B., Duchesne, J.C., Vander Auwera, J., 2006. Magma chamber processes in the Tellnes ilmenite deposit (Rogaland Anorthosite Province, SW Norway) and the formation of Fe-Ti ores in massif type anorthosites. Chem. Geol. 234, 264–290.
Charlier, B., Skår, Ø., Korneliussen, A., Duchesne, J.C., Vander Auwera, J., 2007. Ilmenite composition in the Tellnes Fe–Ti deposit, SW Norway: fractional crystallization, postcumulus evolution and ilmenite–zircon relation. Contrib. Mineral. Petrol. 154, 119–134.
Charlier, B., Sakoma, E., Sauv, M., Stanaway, K., Auwera, J.V., Duchesne, J.C., 2008. The Grader layered intrusion (Havre-Saint-Pierre Anorthosite, Quebec) and genesis of nelsonite and other Fe-Ti-P ores. Lithos 101, 359–378.
Charlier, B., Namur, O., Duchesne, J.C., Wiszniewska, J., Parecki, A., Vander Auwera, J., 2009. Cumulate origin and polybaric crystallization of Fe–Ti oxide ores in the Suwalki Anorthosite, northeastern Poland. Econ. Geol. 104, 205–221.
Charlier, B., Namur, O., Malpas, S., de Marneffe, C., Duschene, J.C., Vander Auwera, J., Bolle, O., 2010. Origin of the giant Allard Lake ilmenite ore deposit (Canada) by fractional crystallization, multiple magma pulses and mixing. Lithos 117, 119–134.
Charlier, B., Namur, O., Bolle, O., Latypov, R., Duchesne, J.-C., 2015. Fe–Ti–V–P ore deposits associated with Proterozoic massif-type anorthosites and related rocks. Earth Sci. Rev. 141, 56–81.
Chen, W., Zhou, M.-F., Zhao, T.-P., 2013. Differentiation of nelsonitic magmas in the formation of the ~1.74 Ga Damiao Fe–Ti–P ore deposit, North China. Contrib. Mineral. Petrol. 165, 1341–1362.
Clift, P.D., Fitton, J.G., 1998. Trace and rare earth element chemistry of volcanic ashes from sites 918 and 919: implications for Icelandic volcanism. In: Saunders, A.D., Larsen, H.C., Wise, S.W. (Eds.), Proc. Ocean Drill. Progr. Sci. Results 152, 67–84.
Condie, K.C., 1997. In: Plate Tectonics and Crustal Evolution, 4th. Butterworth-Heinemann, Oxford Linacre House, pp. 74–90.
Dare, S.A.S., Barnes, S.J., Beaudoin, G., Méric, J., Boutroy, E., Potvin-Doucet, C., 2014. Trace elements in magnetite as petrogenetic indicators. Miner. Deposita 49, 785–796.
Desta, M.T., Ayalew, D., Ishiwatari, A., Arai, S., Tamura, A., 2014. Ferropicrite from the lalibela area in the Ethiopian large igneous province. J. Mineral. Petrol. Sci. 109, 191–207.
Dong, H., Xing, C.M., Wang, C.Y., 2013. Textures and mineral compositions of the Xinjie layered intrusion, SW China: implications for the origin of magnetite and fractionation process of Fe-Ti-rich basaltic magmas. Geosci. Front. 4, 503–515.
Dupuis, C., Beaudoin, G., 2011. Discriminant diagrams for iron oxide trace element fingerprinting of mineral deposit types. Miner. Deposita 46, 319–335.
Eggins, S.M., 1993. Origin and differentiation of picritic arc magmas, Ambae (Aoba), Vanuatu. Contrib. Mineral. Petrol. 114, 79–100.
Eldougdoug, A., Abd El-Rahman, Y., Harbi, H., 2020. The Ediacaran post-collisional Khamal gabbro-anorthosite complex from the Arabian Shield and its Fe-Ti-P ore: an analogy to Proterozoic massif-type anorthosites. Lithos 372–373, 105674.
EMRA, 2014. Mineral resources in the Arab Republic of Egypt: ores of mines, quarries, and salts. The Egyptian Mineral Resources Authority (EMRA) 1, 85–90.
Force, E., 1991. Geology of Titanium-Mineral Deposits. Geological Society of America. Special Paper 259.
Frost, B.R., Lindsley, D.H., 1991. Occurrence of iron-titanium oxides in igneous rocks. In: Lindsley, D.H. (Ed.), Oxide Minerals: Petrologic and Magnetic Significance, vol. 25. Mineralogical Society of America. Reviews in Mineralogy, pp. 433–468.
Gibson, S.A., Thompson, R.N., Dickin, A.P., 2000. Ferropicrites: geochemical evidence for Fe–rich streaks in upwelling mantle plumes. Earth Planet Sci. Lett. 355–374.
Girgis, M.H., 1977. Mineralogical, Petrological and Geochemical Studies on Some Titaniferous Iron Ores of Eastern Desert, Egypt. PhD thesis. Faculty of science, Cairo University, p. 327p.
Goldstein, S.B., Francis, D.M., 2008. The petrogenesis and mantle source of archaean ferropicrites from the western superior province, ontario, Canada. J. Petrol. 49, 1729–1753.
Grammatikopoulos, T., McKen, A., Hamilton, C., Christiansen, O., 2002. A vanadium-bearing magnetite and ilmenite mineralization and beneficiation from the Sinarsuk V-Ti project, West Greenland. Cim. Bull. 95, 87–95.
Green, T.H., Adam, J., 2003. Experimentally determined trace element characteristics of aqueous fluid from dehydrated mafic oceanic crust at 3.0 GPa, 650-700°C. Eur. J. Mineral 15, 815–830.
Guan, J.X., 2014. Petrogenesis of the Panzhihua-type Gabbroic Layered Intrusions and Associated Fe-Ti-V Oxide Deposits: Insights from Mineral Chemistry and Numerical Modeling. University of Tasmania, p. 234. PhD thesis.
Habtoor, A.M., Ahmed, A.H., Al-Akhaly, I.A., Harbi, H.M., Said, N.M., 2022. Orthopyroxene-magnetite symplectites in gabbro of gabal taftafan, western arabian Shield, Saudi Arabia. Arabian J. Geosci. 15, 524.
Haggerty, S.E., 1991. Oxide textures, a mini-atlas. In: Lindesly, D.H. (Ed.), Oxide Minerals, vol. 25. Mineralogical Society of America. Review in Mineralogy, pp. 129–219.
Hart, S.R., Dunn, T., 1993. Experimental Cpx/melt partitioning of 24 trace elements. Contrib. Mineral. Petrol. 113, 1–8.
Hanski, E.J., Smolkin, V.F., 1995. Iron– and LREE–enriched mantle source for early Proterozoic intraplate magmatism as exemplified by the Pechenga ferropicrites, Kola Peninsula, Russia. Lithos 34, 107–125.
Hey, H.M., 1954. A new review of the chlorites. Mineral. Mag. 30, 272–292.
Hinchey, J.G., 2015. The Geology and Genesis of the Keating Hill Fe-Ti-V Prospect, Main Gut Intrusion (NTS Map Areas 12A/05 and 12B/08), Western Newfoundland. Newfoundland and Labrador Department of Natural Resources Geological Survey, pp. 43–61. Report 15-1.
Holness, M., Stripp, G., Humphreys, M., Veksler, I., Nielsen, T., Tegner, C., 2011. Silicate liquid immiscibility within the crystal mush: late-stage magmatic microstructures in the Skaergaard intrusion, East Greenland. J. Petrol. 52, 175–222.
Jang, Y.D., Naslund, H.R., McBirney, A.R., 2001. The differentiation trend of the Skaergaard intrusion and the timing of magnetite crystallisation: iron enrichment revisited. Earth Planet Sci. Lett. 189, 189–196.
Jang, Y.D., Naslund, H.R., 2003. Major and trace element variation in ilmenite in the Skaergaard Intrusion: petrologic implications. Chem. Geol. 193, 109–125.
Johnson, K.T.M., 1998. Experimental determination of partition coefficients for rare earth and high field strength elements between clinopyroxene, garnet and basaltic melt. Contrib. Mineral. Petrol. 133, 60–68.
Karinen, T., Hanski, E., Taipale, A., 2015. The Mustavaara Fe-Ti-V oxide deposit. In: Maier, W.D., O'Brien, H., Lahtinen, R. (Eds.), Mineral Deposits of Finland. Elsevier, Amsterdam, pp. 179–192.
Keevil, H.A., Namur, O., Holness, M.B., 2020. Microstructures and late-stage magmatic processes in layered mafic intrusions: symplectites from the Sept Iles intrusion, Quebec, Canada. J. Petrol. 61 https://doi.org/10.1093/petrology/egaa071.
Khedr, M.Z., Arai, S., Tamura, A., Morishita, T., 2010. Clinopyroxenes in high-P metaperidotites from Happo-O'ne, central Japan: implications for wedge transversal chemical change of slab-derived fluids. Lithos 119, 439–456.
Khedr, M.Z., El-Awady, A., Arai, S., Hauzenberger, C., Tamura, A., Stern, J., Morishita, T., 2020. Petrogenesis of the ~740 ma Korab Kansi mafic-ultramafic intrusion, south Eastern Desert of Egypt: evidence of Ti-rich ferropicritic magmatism. Gondwana Res. 82, 48–72.
Klemm, D.D., Henckel, J., Dehm, R., Von Gruenewaldt, G., 1985. The geochemistry of titanomagnetite in magnetite layers and their host rocks of the eastern Bushveld Complex. Econ. Geol. 80, 1075–1088.
Knipping, J.L., Bilenker, L.D., Simon, A.C., Reich, M., Barra, F., Deditius, A.P., Wälle, M., Heinrich, C.A., Holtz, F., Munizaga, R., 2015. Trace elements in magnetite from massive iron oxide-apatite deposits indicate a combined formation by igneous and magmatic-hydrothermal processes. Geochem. Cosmochim. Acta 171, 15–38.
Kruger, W., Latypov, R.M., 2020. Fossilized solidification fronts in the Bushveld Complex argue for liquid-dominated magmatic systems. Nat. Commun. 11, 2909.
Lattard, D., Saurezapf, U., Kasemann, M., 2005. New calibration data for the Fe-Ti oxide thermo-oxybarometers from experiments in the Fe–Ti–O system at 1 bar, 1000-1300° C and a large range of oxygen fugacities. Contrib. Mineral. Petrol. 149, 735–754.
Latypov, R.M., Chistyakova, S.Yu, Page, A., Hornsey, R., 2016. Field evidence for the in situ crystallization of the Merensky Reef. J. Petrol. 56, 2341–2372.
Latypov, R.M., Chistyakova, S. Yu, Namur, O., Barnes, S., 2020. Dynamics of evolving basaltic magma chambers: textural and chemical evolution of cumulates at the arrival of new liquidus phases. Earth Sci. Rev. 210, 103388, 2020.
Leak, B.E., et al., 1997. Nomenclature of amphiboles: report of the subcommittee on amphiboles of the international mineralogical association, commission on new minerals and mineral names. Am. Mineral. 82, 1019–1037.
Lepage, L.D., 2003. ILMAT: an excel worksheet for ilmenite–magnetite geothermometry and geobarometry. Comput. Geosci. 29, 673–678.
Leterrier, J., Maury, R.C., Thonon, P., Girard, D., Marchal, M., 1982. Clinopyroxene composition as a method of identification of the magmatic affinities of paleo-volcanic series. Earth Planet Sci. Lett. 59, 139–154.
Lindsley, D.H., 1983. Pyroxene thermometry. Am. Mineral. 68, 289–339.
Liu, P.P., Zhou, M.F., Chen, W.T., Gao, J.F., Huang, X.W., 2015. In-situ LA-ICP-MS trace elemental analyses of magnetite: Fe–Ti–(V) oxide-bearing mafic-ultramafic layered intrusions of the Emeishan Large Igneous Province, SW China. Ore Geol. Rev. 65, 853–871.
Luan, Y., Song, X.Y., Chen, L.M., Zheng, W.Q., Zhang, X.Q., Yu, S.Y., She, Y.W., Tian, X. L., Ran, Q.Y., 2014. Key factors controlling the accumulation of the Fe–Ti oxides in the Hongge layered intrusion in the Emeishan Large Igneous Province, SW China. Ore Geol. Rev. 57, 518–538.
Lustrino, M., 2006. Composition, petrography and mineral chemistry of ODP site 1224 eocene ferrobasalts (leg 200; north Pacific ocean). In: Kasahara, J., Stephen, R.A., Acton, G.D., Frey, F.A. (Eds.), Proceedings of the Ocean Drilling Program, vol. 200. Scientific Results, pp. 1–36.
Maila, R.P., 2015. Geochemistry of Magnetitite Layers in the Upper Zone of the Bushveld Complex, South Africa. University of the Witwatersrand, Johannesburg, p. 128p. M. Sc thesis.
Makhlouf, A., Beniamin, N.Y., Mansour, M.M., Mansour, S.A., El-Shrbeni, H., 2008. Mafic-ultramafic intrusion of south Korab Kansi area with emphasis on titanomagnetite ores, south Eastern desert, Egypt. Ann. Geol. Surv. Egypt 3, 1–20.
Martin, D., 1990. Crystal settling and in situ crystallization in aqueous solutions and magma chambers. Earth Planet Sci. Lett. 96, 336–348.
McBirney, A.R., Noyes, R.M., 1979. Crystallization and layering of the Skaergaard intrusion. J. Petrol. 20, 487–554.
McDonough, W.F., Sun, S.S., 1995. The composition of the Earth. Chem. Geol. 120, 223–253.
Mallmann, G., O'Neill, H.S.C., 2009. The crystal/melt partitioning of V during mantle melting as a function of oxygen fugacity compared with some other elements (Al, P, Ca, Sc, Ti, Cr, Fe, Ga, Y, Zr and Nb). J. Petrol. 50, 1765–1794.
Merle, O., 2011. A simple continental rift classification. Tectonophysics 513, 88–95.
Morimoto, N., Fabries, J., Ferguson, A.K., Ginzburg, I.V., Ross, M., Seifert, F.A., Zussman, J., Gottardi, D., 1988. Nomenclature of pyroxenes. Am. Mineral. 62, 53–62.

Morisset, C.E., 2008. Origin of Rutile-Bearing Ilmenite Fe–Ti Deposits in Proterozoic Anorthosite Massifs of the Grenville Province. Ph.D. Thesis. Univ. British Columbia, Vancouver, British Columbia, p. 301.
Morisset, C.E., Scoates, J.S., Weis, D., Sauvé, M., Stanaway, K.J., 2010. Rutile-bearing ilmenite deposits associated with the Proterozoic saint-Urbain and lac allard anorthosite massifs, Grenville province, Quebec. Can. Mineral. 48, 821–849.
Nadoll, P., Angerer, T., Mauk, J.L., French, D., Walshe, J., 2014. The chemistry of hydrothermal magnetite: a review. Ore Geol. Rev. 61, 1–32.
Namur, O., Charlier, B., Toplis, M.J., Higgins, M.D., Liégeois, J.P., Vander Auwera, J., 2010. Crystallization sequence and magma chamber processes in the ferrobasaltic Sept Iles layered intrusion, Canada. J. Petrol. 51, 1203–1236.
Namur, O., Charlier, B., Pirard, C., Hermann, J., Liégeois, J.P., Vander Auwera, J., 2011. Anorthosite formation by plagioclase flotation in ferrobasalt and implications for the lunar crust. Geochem. Cosmochim. Acta 75, 4998–5018.
Namur, O., Charlier, B., Holness, M.B., 2012. Dual origin of Fe–Ti–P gabbros by immiscibility and fractional crystallization of evolved tholeiitic basalts in the Sept Iles layered intrusion. Lithos 154, 100–114.
Nasr, B.B., Sadek, M.F., Masoud, M.S., 2000. Some new occurrences of layered titanomagnetite, Eastern Desert, Egypt. Ann. Geol. Surv. Egypt XXIII, 679–690.
Nimis, P., Vannucci, R., 1995. An ion microprobe study of clinopyroxenes in websteritic and megacrystic xenoliths from Hyblean Plateau (SE Sicily, Italy): constraints on HFSE/REE/Sr fractionation at mantle depth. Chem. Geol. 124, 185–197.
Nisbet, E.G., Pearce, J.A., 1977. Clinopyroxene composition in mafic lavas from different tectonic settings. Contrib. Mineral. Petrol. 63, 149–160.
Pang, K.N., Zhou, M.F., Lindsley, D., Zhao, D., Malpas, J., 2008. Origin of Fe-Ti oxide ores in mafic intrusions: evidence from the Panzhihua intrusion, SW China. J. Petrol. 49, 295–313.
Pearce, N.J., Perkins, W.T., Westgate, J.A., Gorton, M.P., Jackson, S.E., Neal, C.R., Chenery, S.P., 1997. A compilation of new and published major and trace element data for NIST SRM 610 and NIST SRM 612 glass reference materials. Geostand. Newsl. 21, 115–144.
Philpotts, A.R., 1967. Origin of certain iron–titanium oxide and apatite rocks. Econ. Geol. 62, 303–315.
Ramdohr, P., 1980. In: The Ore Minerals and Their Intergrowths, second ed.s. Pergamon press, Oxford, p. 2005.
Ramsay, W.R.H., Crawford, A.J., Foden, J.D., 1984. Field setting, mineralogy, chemistry, and genesis of arc picrites, New Georgia, Solomon Islands. Contrib. Mineral. Petrol. 88, 386–402.
Ripley, E.M., Severson, M.J., Hauck, S.A., 1998. Evidence for sulfide and Fe-Ti-P-rich liquid immiscibility in the Duluth complex, Minnesota. Econ. Geol. 93, 1052–1062.
Sabet, A.H., Khalaf, I.M., 1989. Petrological, mineralogical and geochemical studies on magnetite-ilmenite-apatite ore (Nelsonite) from Kolminab, south Eastern desert UAR. The proceed Egypt Academic Science 22, 235–440.
Schmidt, M.W., 1992. Amphibole composition in tonalities as a function of pressure: an experimental calibration of the Al-in-hornblende barometer. Contrib. Mineral. Petrol. 110, 304–310.
Schuiling, R.D., Feenstra, A., 1980. Geochemical behaviour of vanadium in iron-titanium oxides. Chem. Geol. 30, 143–150.
Scoon, R., Costin, G., Jan Grabe, P., 2017. Geology and origin of the Vanadiferous Fe-Ti oxide-rich Kennedy's Vale discordant body, eastern limb of the Bushveld complex, South Africa. S. Afr. J. Geol. 120, 251–270.
Shaaban, G.M., Botros, N.S.H., Oweis, K.H.A., Eissa, M.E., Aly, K.M., Hassan, A.A., 2003. Titaniferous iron ore of Wadhait area, south Eastern Desert, Egypt. In: 41th Annual Conference of Geological Society of Egypt, Cairo, Egypt.
Shellnutt, J.G., Pang, K.N., 2012. Petrogenetic implications of mineral chemical data for the Permian Baima igneous complex, SW China. Mineral. Petrol. 106, 75–88.
Song, X.Y., Qi, H.W., Hu, R.Z., Chen, L.M., Yu, S.Y., Zhang, J.F., 2013. Formation of thick stratiform Fe-Ti oxide layers in layered intrusion and frequent replenishment of fractionated mafic magma: evidence from the Panzhihua intrusion, SW China. G-cubed 14, 712–732.
Spandler, C., Mavrogenes, J., Hermann, J., 2007. Experimental constraints on element mobility from subducted sediments using high-P synthetic fluid/melt inclusions. Chem. Geol. 239, 228–249.
Stromer Jr., J.C., 1983. The effects of recalculation on estimates of temperatures and oxygen fugacity from analyses of multicomponent iron-titanium oxides. Am. Mineral. 68, 586–594.
Stosch, H.G., 1982. Rare earth partitioning between minerals from anhydrous spinel peridotite xenoliths. Geochem. Cosmochim. Acta 46, 793–811.
Sun, S.S., McDonough, W.F., 1989. Chemical and isotopic systematics of oceanic basalts: implications for mantle composition and processes. In: Saunders, A.D., Norry, M.J. (Eds.), Magmatism in the Ocean Basins, vol. 42. Geological Society, pp. 313–345.
Surour, A.A., Ahmed, A.H., Harbi, H.M., 2017. Mineral chemistry as a tool for understanding the petrogenesis of Cryogenian (arc-related) Ediacaran (post-collisional) gabbros in the western Arabian Shield of Saudia Arabia. Int. J. Earth Sci. 106, 1597–1617.
Taipale, A., Tutkielma, P., Laitos, G., Yliopisto, O., 2013. Composition of Magnetite in Gabbros of the Mustavaara. University of Oulo, p. 59. M.Sc thesis.
Tan, W., Wang, C.Y., He, H.P., Liang, X.L., Liu, P., 2016. Mineralogy and origin of exsolution in the titanomagnetite of different magmatic Fe-Ti oxide bearing intrusions. Can. Mineral. 54, 539–553.
Toplis, M.J., Corgne, A., 2002. An experimental study of element partitioning between magnetite, clinopyroxene and iron-bearing silicate liquids with particular emphasis on vanadium. Contrib. Mineral. Petrol. 144, 22–37.
Tuff, J., Takahashi, E., Gibson, S.A., 2005. Experimental constraints on the role of garnet pyroxenite in the genesis of high-Fe mantle plume derived melts. J. Petrol. 46, 1–36.
Turnock, A., Eugster, H., 1962. Fe-Al Oxides: phase relationships below 1000°C. J. Petrol. 3, 533–565.
Valvasori, A.A., Hanchar, J.M., Piercey, S.J., Fonkwe, M.L.D., 2020. The origin and evolution of V-rich, magnetite dominated Fe-Ti oxide mineralization; Northwest River Anorthosite, south-central Labrador, Canada. Miner. Deposita 55, 555–575.
Von Gruenewaldt, G., 1993. Ilmenite–apatite enrichment in the upper zone of the Bushveld complex: a major titanium–rock phosphate resource. Int. Geol. Rev. 35, 987–1000.
Vincent, E., Wright, J., Chevallier, R., Mathieu, S., 1957. Heating experiments on some natural titaniferous magnetite. Mineral. Mag. 31, 624–655.
Wang, C.Y., Zhou, M.F., Zhao, D.G., 2008. Fe-Ti-Cr oxides from the Permian Xinjie mafic-ultramafic layered intrusion in the Emeishan large igneous province, SW China: crystallization from Fe- and Ti-rich basaltic magmas. Lithos 102, 198–217.
Wang, C.Y., Zhou, M.-F., Yang, S., Qi, L., Sun, Y., 2014. Geochemistry of the Abulangdang intrusion: cumulates of high-Ti picritic magmas in the Emeishan large igneous province, SW China. Chem. Geol. 378, 24–39.
Woodland, S.J., Pearson, D.G., Thirlwall, M.F., 2002. A platinum group element and Re–Os isotope investigation of siderophile element recycling in subduction zones: comparison of Grenada, Lesser Antilles arc, and the Izu-Bonin arc. J. Petrol. 43, 171–198.
Zhang, Z.C., Mao, J.W., Saunders, A.D., Ai, Y., Li, Y., Zhao, L., 2009. Sr, Nd, Pb and O isotopes of clinopyroxenes from the three typical mafic–ultramafic layered intrusions in the Emeishan large igneous province, SW China. Lithos 113, 369–392.
Zhang, X.Q., Song, X.Y., Chen, L.M., Xie, W., Yu, S.Y., Zheng, W.Q., Deng, Y.F., Zhang, J. F., Gui, S.G., 2012. Fractional crystallization and the formation of thick Fe-Ti-V oxide layers in the Baima layered intrusion, SW China. Ore Geol. Rev. 49, 96–108.
Zhou, M., Robinson, P., Lesher, M., Keays, R., Zhang, C., Malpas, J., 2005. Geochemistry, Petrogenesis and metallogenesis of the Panzhihua gabbroic layered intrusion and associated Fe–Ti–V oxide deposits, Sichuan Province, SW China. J. Petrol. 47, 2253–2280.